Research article

JGS
Journal of the Geological Society

https://doi.org/10.1144/jgs2025-005 | Vol. 182 | 2025 | jgs2025-005

The role of sill intrusion in delimiting the lateral propagation of giant dyke swarms: emplacement of the Dogger Sill Complex, Southern North Sea

Joe Cartwright*, **Martino Foschi and Daniel Phillips**

Department of Earth Sciences, University of Oxford, South Parks Road, Oxford OX1 3AN, UK
JC, 0000-0003-4198-9719; MF, 0000-0002-0360-7719; DP, 0009-0004-9250-8852
* Correspondence: joe.cartwright@earth.ox.ac.uk

Abstract: This study addresses the question of which factors control the lateral arrest of giant dykes. We present new seismic mapping of a large sill complex associated with the distal portion of the Mull Dyke Swarm in the Southern North Sea, which we name the Dogger Sill Complex. Fifteen key calibration wells show that dolerite sills ranging from 20 to 98 m thick intrude into potash-rich units of the Z3 cycle of the Zechstein Group. We mapped six main sills intruded within 5 km of three of the longest dykes belonging to the Mull Dyke Swarm, suggesting that these dykes fed the sills. The sills have a combined area of 429 km^2 and a median gross volume of *c.* 22.7 km^3. Their concordant intrusion into the potash-rich Z3K unit implies that the physical properties of this unit exerted a primary control on sill emplacement. Intrusion of the sill complex is argued to have impacted the propagation of the dykes and contributed to their arrest only 50 km beyond the limit of the sills via the loss of the driving magma pressure. The intrusion of a large sill complex so close to the terminus of a giant dyke swarm may be a more widely developed mechanism for lateral dyke arrest than currently appreciated.

Received 9 January 2025; **revised** 4 March 2025; **accepted** 5 March 2025

Giant dyke swarms are important, but enigmatic, components of many large igneous provinces with their capacity to transmit large volumes of magma laterally over vast distances (White 1992; Ernst *et al.* 1995). They have been recognized widely on Earth, Venus and Mars (Head *et al.* 1992; Parfitt and Head 1993; Ernst *et al.* 1995; Mège and Masson 1996; Ernst and Buchan 1997; Scott *et al.* 2002) and may even be responsible for the largest magma effusion rates on record (Fialko and Rubin 1999).

Individual dykes within giant dyke swarms commonly exceed lengths of 100 km and, in numerous cases, exceed 1000 km (El Bilali and Ernst 2024). These extraordinary dimensions for what are essentially fractures driven by magma pressure prompt questions regarding the controls on the lateral propagation of such fractures in the crust of the terrestrial planets and how this propagation is regulated. Long-range lateral propagation requires that the dykes in question do not approach the surface sufficiently closely with enough magma pressure to erupt. If a vigorous eruption were to take place, it would deplete the magma supply required for the dyke to continue propagating laterally (Ernst *et al.* 1995; Parfitt and Wilson 2009). A good example of such a case is the Bárðarbunga intrusion in Iceland in 2014, where, after *c.* 50 km of lateral propagation beneath the surface, a fissure eruption at the distal limit of the dyke resulted in its arrest (Gudmundsson *et al.* 2014; Woods *et al.* 2019).

Contrasting factors have been proposed to explain why the lateral propagation of dykes is arrested in examples where no terminal eruption occurs. Most theoretical contributions suggest that lateral propagation may be delimited by: (1) declining magma pressure in the magma source (e.g. magma chamber); (2) termination of the magma supply from the source; (3) obstruction by a mechanical or stress barrier, such as structures or rock masses, the stress intensity factor of which exceeds the critical value for tensile failure at the advancing dyke tip; or (4) pressure losses within the dyke itself (e.g. Lister and Kerr 1991; Ernst *et al.* 1995; Rubin 1995; Rivalta *et al.* 2015). Less commonly, it has been suggested that cooling and an increase in the viscosity of the magma at the distal tips might lead to dyke arrest (Delaney and Pollard 1982; Macdonald *et al.* 1988; Fialko and Rubin 1999). It does not appear to have been suggested previously that the diversion of the magma supply from the propagating dyke into, for example, a sill intrusion could also play a part in leading to dyke arrest.

We explore here the possibility that sills fed by laterally propagating dykes may divert enough of the gross magma supply to the lateral tips such that lateral propagation terminates sooner than it otherwise would have done. We do so by presenting the first detailed maps of a buried sill complex that straddles the UK–Netherlands border in the Southern North Sea, hosted within Late Permian evaporites (the Zechstein Group). The aim of this paper is to present the results of the subsurface mapping of this sill complex, which is intruded along the axes of the major dykes of the central group of the Mull Dyke Swarm (MDS). The focus of this paper is the detailed description of this newly identified sill complex (termed here the Dogger Sill Complex) and its relationship with the major dykes. We conclude with a discussion of the possible emplacement mechanisms and the implications of the intrusion of sills for the overall evolution of the MDS and for the questions relating to the limits to the lateral propagation of giant dyke swarms more generally.

Geological context of the Dogger Sill Complex

Sill intrusions into the Zechstein Group in the Southern North Sea were first identified by Gauer *et al.* (2004) based on a careful examination of petrophysical data from four petroleum exploration boreholes combined with interpretation and modelling of high-resolution aeromagnetic data. Their analysis was based on a small area of the UK Sector, close to the international median line, but did not include any direct mapping of the sills identified in boreholes on either 2D or 3D seismic data. Gauer *et al.* (2004) did, however, connect the emplacement of the sills they identified to the propagation of the MDS, which had earlier been mapped closer to

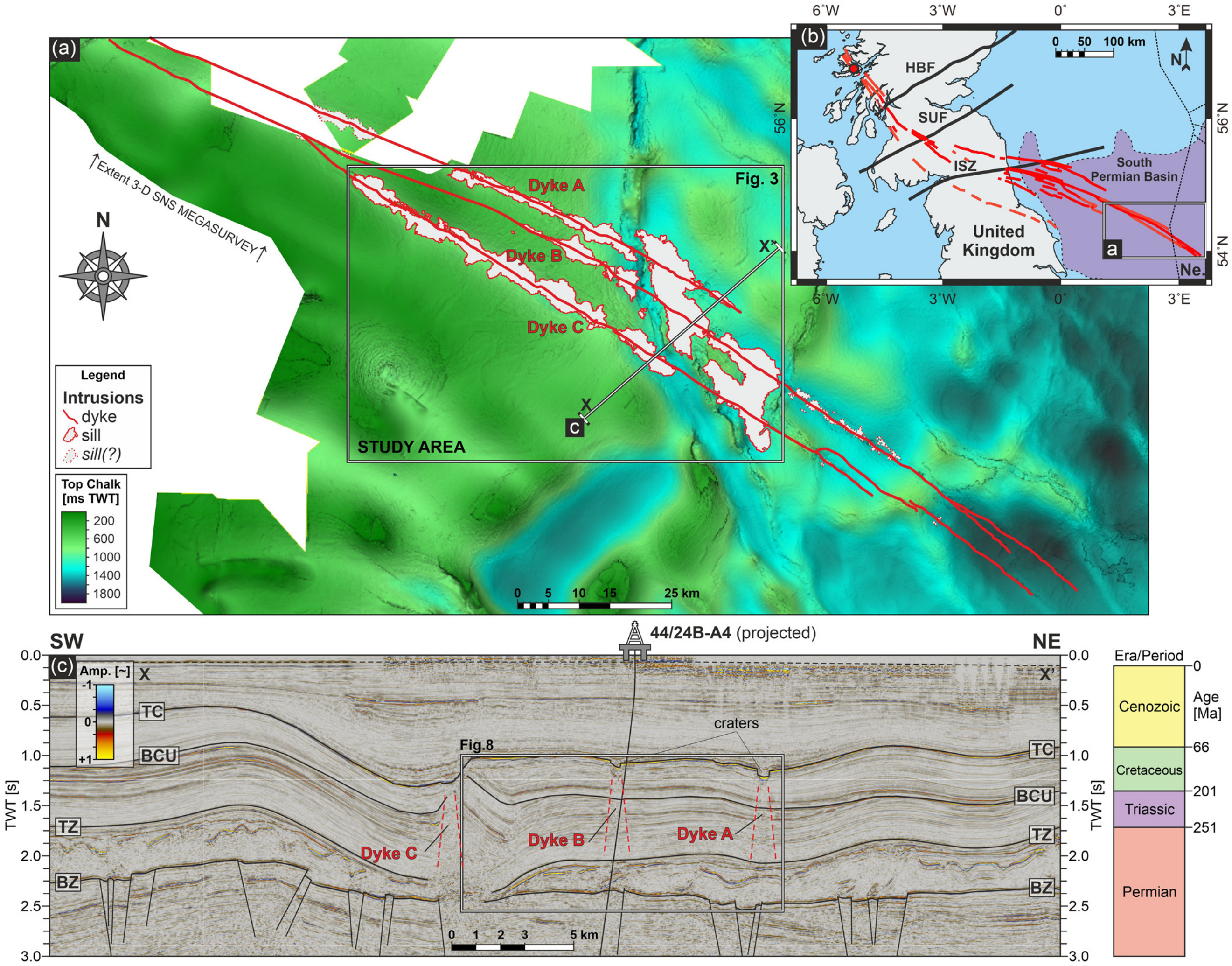

Fig. 1. (**a**) Outline map of the Mull Dyke Swarm as mapped in the onshore and offshore areas over which it extends. The outline of the South Permian Basin is indicated by the boundaries of the platform and basin settings for the Z2 Zechstein cycle. (**b**) Location of the study area within the Silverpit Basin overlain on a two-way travel time structure map of the Top Chalk horizon. This map was constructed from the SNS Megamerge 3D seismic survey (see text) and shows the main salt tectonic structures in the area, including a prominent set of salt-cored folds and a NNW-trending salt wall located towards the eastern end of the study area. The outline of the sills mapped in this study is shown for reference (see Fig. 3 for details), along with the mapped positions of the main dykes of the central group of the Mull Dyke Swarm (dykes A, B and C). (**c**) Representative regional seismic profile across the study area showing the salt tectonic structural style of the area, the main stratigraphic unit geometries (including a generalized stratigraphic column) and the three main dykes in the area. Well trajectory for well 44/24b-A4 shown for reference (see Fig. 7 for details). Dashed red lines indicate boundaries of the seismic disturbance zones associated with the dykes. The regionally mapped horizons shown are the: BZ, Base Zechstein; TZ, Top Zechstein; BCU, Base Cretaceous Unconformity; TC, Top Chalk. HBF, Highland Boundary Fault; ISZ, Iapetus Suture Zone; SDZs, seismic disturbance zones; SUF, Southern Uplands Fault. Source: map in part (a) adapted from Carver *et al.* (2023), with the boundaries of the South Permian Basin from Grant *et al.* (2019). The locations of dykes A, B and C in part (b) are from Carver *et al.* (2023).

the coast of NE England using seismic and aeromagnetic data by Kirton and Donato (1985) and Brown *et al.* (1994). Subsequently, only one other geophysical study has reported the possible occurrence of a sill along the axis of the MDS, but without confirmation from drilling results (Wall *et al.* 2010).

Our study is based on a review of >100 wells in the UK Sector of the southern Permian Basin using the same approach as described by Gauer *et al.* (2004) to identify possible sills from petrophysical data and lithological samples. We extended the search region to cover all the wells within 20 km of the dykes comprising the central group of the MDS as mapped across the Southern North Sea by Carver *et al.* (2023) (Fig. 1). The rationale for defining our search region was based on the arguments presented by Gauer *et al.* (2004) and Wall *et al.* (2010) that the sills were fed by the dykes comprising the MDS. The primary scope of our study was to identify sills in as many wells as possible and, through careful petrophysical calibration of the wells with the seismic data, to construct detailed maps of the sills using the resolving power of open-file 3D seismic data.

The Dogger Sill Complex is located at the distal limits of the MDS (Fig. 1). The MDS has been classified as a giant dyke swarm based on its dimensions and relationship with its source area (Ernst *et al.* 1995; Magee *et al.* 2019). The MDS has been recognized as a major feature of the British and Irish Paleogene Igneous Province for over a century, mainly from classical field-based studies in southern Scotland and northern England (Geikie 1897; Tyrrell 1917; Richey 1939). Petrological and geochemical fingerprinting has confirmed a match between the composition of the dykes and their source magma types on Mull (Holmes and Harwood 1929; Macdonald *et al.* 1988; Ishizuka *et al.* 2017). In the last two decades, the availability of subsurface databases acquired for gas exploration in the Southern North Sea has facilitated the mapping of the MDS beyond the limits of the surface outcrops for an additional 300 km into Dutch waters (Kirton and Donato 1985; Brown *et al.*

1994; Wall *et al.* 2010; Underhill 2009; Carver *et al.* 2023) (Fig. 1). The most distal dykes within the swarm thus extend *c.* 670 km from their origin on Mull (Carver *et al.* 2023).

The ESE-propagating MDS transects a range of basement domains, major crustal-scale fault zones and sedimentary basins of different ages from its source to its terminus in the Southern North Sea (Fig. 1). In our study area of the Southern North Sea, the dykes intrude Paleozoic and Mesozoic sedimentary rocks of various lithologies and degrees of induration and deformation (Fig. 1c). The Paleozoic sediments were deposited in small extensional sub-basins as part of a wider network of rifting from the Devonian into the Late Carboniferous, culminating in strong uplift and erosion during the Variscan Orogeny (Glennie 1986; Ziegler 1990; Corfield *et al.* 1996; Besly 2019). Variscan deformation was followed by a period of tectonic relaxation in the Permian, during which the North and South Permian basins became established with generally east–west-trending axes of regional subsidence and little to no active fault-controlled subsidence (Ziegler 1990). The Late Permian was a period of limited clastic deposition in a generally arid climate, but subsidence promoted the development of four main carbonate–evaporite cycles (Z1–Z4), each of which exhibits large lateral continuity, with correlative units stretching from NE England to Poland (Stewart 1963; Smith 1979; Richter-Bernburg 1986; Cameron *et al.* 1992; Taylor 1998).

The Mesozoic history of the Southern North Sea region is complex, with a superposition of minor rifting events, halokinesis of the thick underlying Zechstein evaporites and regional subsidence (Ziegler 1990). This combination has led to significant deformation of the Mesozoic units, with erosional truncation in places and the initial development of salt walls and pillows (Jenyon 1988). The final shaping of the geology of the study area during the Cenozoic involved thin- and thick-skinned contractional tectonics in the Paleogene, leading to the development of major salt-cored folds across much of the basin axis (Hughes and Davison 1993; Stewart and Coward 1995; Wall *et al.* 2010; Underhill 2009). A major regional eastward tilting of the basin and uplift and erosion of the western basin margin, culminating in the Mid-Miocene Unconformity, led to preservation of the MDS eastwards and progressively deeper erosion levels of the dykes westwards. Nevertheless, a *c.* 250 km long section of the MDS is fully preserved, with its upper tips intact beneath an uneroded Cenozoic cover (Fig. 1c) (Carver *et al.* 2023).

The stratigraphic relationships of erosional truncation and onlap fill in a series of craters developed above the preserved upper tips of the dykes suggest a Late Paleocene age for dyke intrusion (Wall *et al.* 2010; Carver *et al.* 2023; Pryce *et al.* 2025). This biostratigraphically constrained age is consistent with the limited radiometric dating of constituent dykes from the MDS on land, which places the timing of intrusion at *c.* 59–58 Ma during chron C26R (Evans *et al.* 1973; Mitchell *et al.* 1989). This is also consistent with the exclusively negative magnetization of the dykes (Kirton and Donato 1985; Chambers and Pringle 2001). The timing of intrusion post-dates the early halokinetic structures in the basin (Jenyon 1988; Cameron *et al.* 1992), but predates the widespread development of salt-cored folds (Hughes and Davison 1993; Stewart and Coward 1995; Wall *et al.* 2010).

Previous studies of the dykes in the Southern North Sea using 3D seismic data have recognized that they are not directly imaged due to their steeply dipping to vertical attitude, but they can nevertheless be mapped in the form of seismic disturbance zones (SDZs) (Fig. 2). These SDZs often underlie crater-like features identified by various studies developed within the uppermost Chalk Group sediments and it is the scattering effect, combined with seismic velocity anomalies associated with these craters, that causes the SDZs (Wall *et al.* 2010; Carver *et al.* 2023; Pryce *et al.* 2025).

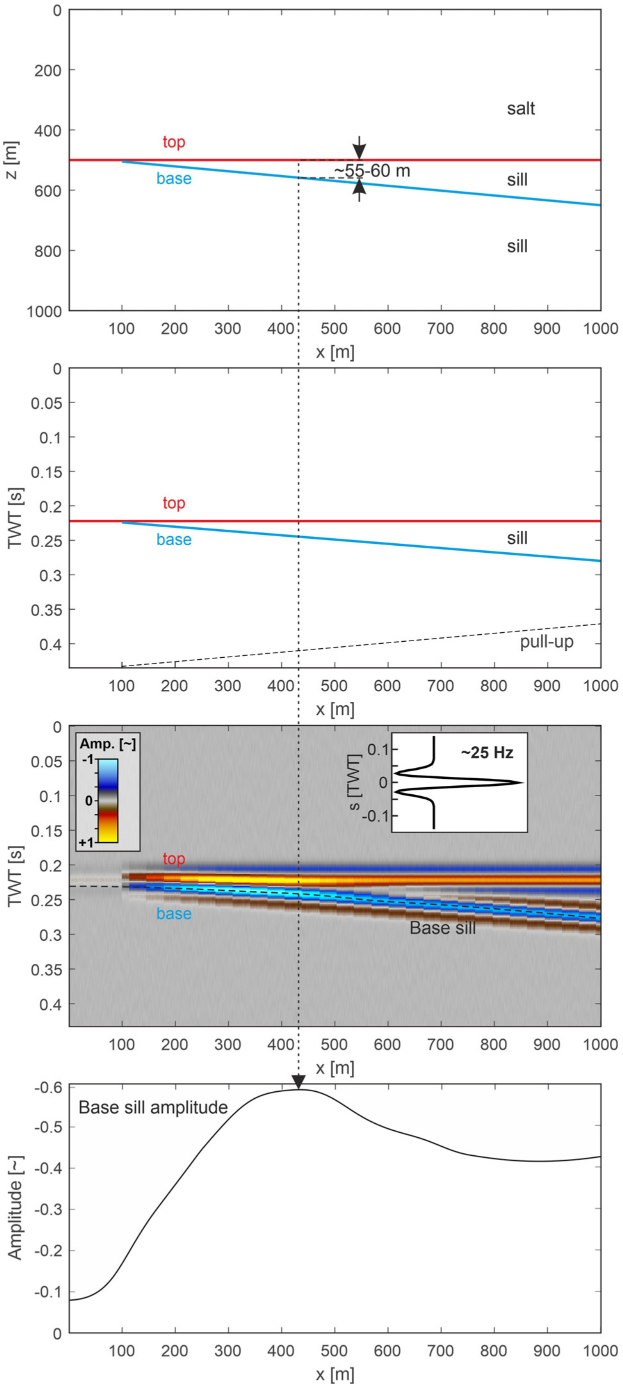

Fig. 2. Wedge model constructed to evaluate the tuning and resolution of dolerite sills embedded in halite. The velocity values obtained from calibration wells used for dolerite and halite were 5250 and 4400 m s^{-1}, respectively. (**a**) Depth section with an idealized wedge geometry of a dolerite sill. (**b**) Time converted profile for the wedge. (**c**) Convolution of the wedge with a zero-phase Ricker wavelet (dominant frequency 25 Hz) showing the classical response of the wedge with strong amplification of the upper (positive peak) and lower (negative peak) reflections close to the tuning position. (**d**) Dimensionless amplitude v. distance along the wedge for the base sill reflection showing a broad peak centred between 370 and 470 m, giving a tuning thickness of 55–60 m.

Data and methods

3D seismic data

A combination of 3D seismic and well data was used to identify and map sills within the study area and to interpret their relationships with the host stratigraphy, structure and igneous dykes in the UK

Sector of the South Permian Basin. The seismic data used in this study are the Southern North Sea 3D Seismic MegaSurvey (SNS MegaSurvey) processed by PGS UK Ltd and released under academic licence from Petroleum Geo-Service and made available via the North Sea Transition Authority (NSTA). The SNS MegaSurvey has a lateral extent of 67 253 km^2 and is the result of the merging of >200 individual 3D surveys. These individual 3D surveys have different acquisition histories dating back to 1998. The data were finalized to a 4 ms two-way travel time (TWT) interval and interpolated to a 25 m bin spacing in both the IN-lines and X-lines (PGS Reservoir 2016).

The frequency spectrum of the SNS MegaSurvey within the interval of interest from 1500 to 2500 ms TWT is characterized in the study area by a central (dominant) frequency of *c.* 25 Hz, with a bandwidth of 18–32 Hz above −1 dB. The data in this interval were analysed using Petrel's wavelet toolbox and was found to be zero phase with a positive acoustic impedance contrast characterized by a positive peak response.

Vertical resolution and wedge models

The vertical resolution is an important factor in the interpretation of sill intrusions using seismic data, particularly when it is suspected that the thickness range may overlap with the tuning thickness (Smallwood and Maresh 2002; Köpping *et al.* 2022). The vertical resolution of the SNS MegaSurvey was assessed using wedge modelling (Widess 1973; Brown 2011) and was specifically constructed based on the rock properties of halite and dolerite as derived from wells in the study area (Fig. 2). The wedge model included a dolerite wedge with a density of 2650 kg m^{-3} and a velocity of 5250 m s^{-1}, overlain by a thick layer of halite with a density of 2150 kg m^{-3} and a velocity of 4400 m s^{-1}. The halite below the wedge was characterized by a density of 2250 kg m^{-3} and a velocity of 4500 m s^{-1}. The reflection coefficients were calculated using a standard normal incidence acoustic impedance contrast equation in which the reflection coefficient, *RC*, was defined as

$$RC = \frac{Vp_{i+1}\rho_{i+1} - Vp_i\rho_i}{Vp_{i+1}\rho_{i+1} + Vp_i\rho_i},$$

and where the product $Vp_i\rho_i$ is the acoustic impedance of rock *i*. The RC model was then converted to TWT using the velocities previously defined and then convolved with a nominal Ricker wavelet characterized by the characteristic frequency (25 Hz), phase (zero) and polarity (RC+ peak) of the 3D seismic data. The wedge model, using the amplitude response of the base wedge, reveals that the tuning amplification occurs for a sill thickness of 55–60 m. This important parameter will be used as a benchmark in the following description and discussions about the acoustic features of the sill intrusions encountered in the study area.

Well database

The well database used in this study consists of >100 wells spread across the study area (Fig. 3, Table 1). A subset of 60 wells was studied to characterize the Zechstein stratigraphy, while 15 penetrated igneous intrusions (both dykes and sills) or the altered remnants of igneous intrusions. Data extracted from the archive included completion and petrophysical logs (particularly gamma

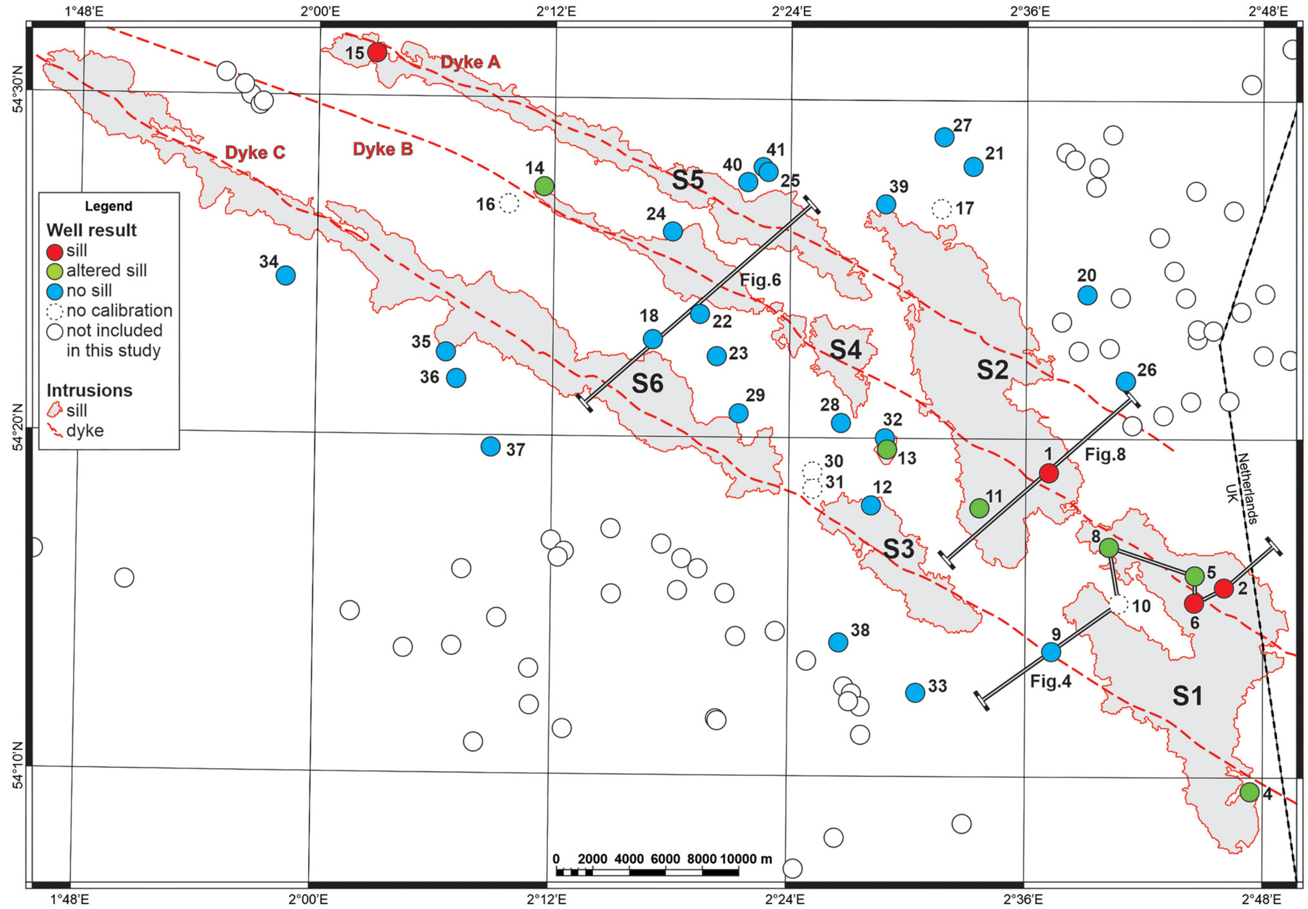

Fig. 3. Location map of the study area (see Fig. 1 for basinal context) showing the outline and nomenclature of the six sills mapped in the main study area (for details, see text). The grid for the UK Exploration Licence Blocks is shown along with the UK/Netherland median line. The wells used in the study (numbered) are identified in Table 1. The colour coding for the wells indicates which type of sill intrusion they intersected or whether there was no intersection. Source: the mapped positions of dykes A, B and C are from Carver *et al.* (2023).

Table 1. List of wells used in this study

	Well		Intrusion			Z4	Z3		
No. in Figure 3	Quadrant	Name	Type	Thickness (m)	V_p (m s^{-1})	Thickness (m)	Thickness (m)	K-salt N/G (%)	K-salt thickness (m)
	42	10-1							
		10b-2Z							
		10b-2							
	43	15b-3A				93.26			
		1-6					12.19	60	7.31
34		20b-2				122.22			
		20-1	Not calibrated						
		08-1	Not calibrated						
		07-1	Not calibrated						
		06-1							
		19-1				127.1			
		19C-1				130			
		02-1							
	44	11-1				97.23			
		11-2				79.85			
		11-3	Sill	98.75	5143.6	33.83			
		11a-4					45.72	25	11.43
		12-2					91.44	20	18.28
		12a-4					36.57	15	5.48
		12a-6					58.21	35	20.37
15		16-1ZCT				115.21			
36		16-2				142.03	42.67	5	2.13
35		**16-3**	Altered sill (?)			110.64	49.37	15	7.4
14		16a-4	No calibration						
16		16a-4z							
		17-1				122.22			
23		17-2				122.83	53.64	20	10.72
22		17-3					21.33	10	2.13
25		17a-4				101.19			
41		17a-5				131.67	26.21	10	2.62
18		17a-6				135.94	85.34	30	25.6
40		17b-7				109.72			
24		17c-m1							
29		17c-m^2							
		18-1	Weld, no calibration						
17		18-2							
27		18-3					57.91	20	11.58
28		18-T3A							
39		18a-5					76.2	10	7.62
21		18b-K1	Sill	29.91		97.53			
		19-4					30.48	30	9.14
		19a-5					82.29	10	8.22
		19a-8					54.25	40	21.7
32		19b-6				109.72	107.28	45	48.28
20		19b-7				134.41			
26		19b-7a					26.21	40	10.48
		21-5					137.16	30	41.14
		21a-6					103.63	25	25.9
		21a-9					48.76	30	14.63
		21a-10					82.29	30	24.68
		21b-8							
		22-1					51.81	20	10.36
		22-3				125.88	98.75	30	29.62
		22-5					109.72	15	16.45
		22-7					156.05	35	54.62
37		23-4				111.86	18.28	40	7.31
38		23-6				115.82	112.77	30	33.83
		23-7					9.14	70	6.4
		23-8					27.43	30	8.22
		23-9					57.91	30	17.37
33		23a-8				171.01			

(continued)

Table 1. *Continued*

	Well		Intrusion			Z4	Z3			
No. in Figure 3	Quadrant	Name	Type	Thickness (m)	V_p (m s^{-1})	Thickness (m)	Thickness (m)	K-salt N/G (%)	K-salt thickness (m)	
12		23a-10	Not calibrated							
30		23a-12	Not calibrated							
31		**23b-11**	Altered sill	38.71		96.92	12.19	3	0.36	
		23b-15					24.38	15	3.65	
13		**23b-13**	Altered sill	45.11		103.63				
11		**23g-14**	Sill	69.01		98				
		23g-15								
		24-1	Not calibrated							
10		**24-2**	Altered sill	20.11		113.99				
8		24-3								
9		24-4	Altered sill (?)	80.77		87.78				
5		24-5a	Sill	47	5215.5	105.46				
		24a-6	Sill	48.16	5500	102.41				
6		24a-6Y	No sill							
7		24b-13	Altered sill (?)							
		24b-7Z	Altered sill (?)	54.02		101.01				
		24b-A2	Sill	53.99		105.99				
		24b-A2Z								
		24b-A3	Sill	68.01		110.01				
44		24b-a4	Dyke and sill	45.99		113				
1		24b-A5	Sill	20		125				
2		24b-a6	Sill	83		81				
		28-3					60.96	30	18.28	
		28-4					67.05	10	6.7	
		29-3					85.34	30	25.6	
3		29b-4	Altered sill (?)			124.97				
				15	3	37	36	36	36	N
				48.16	5215.5	110.64	56.08	30	11.075	mean
				53.50266667	5286.366667	111.0902703	61.6925	26.19444444	15.98916667	median

Data extracted from completion reports including well name, details on intrusion thickness, seismic velocity, thicknesses of Z3 and Z4 cycles and potash occurrences in Z3K. Number in figure refers to numbering of wells in Fig. 3. N/G, Net-to-gross.

ray, resistivity, sonic velocity and density logs). Well-to-seismic ties were undertaken using depth-to-time calibration exclusively derived from vertical seismic profiles downloaded from the NSTA archive (see Results section for details). Errors in tying specific lithological boundaries to seismic marker horizons were estimated at ±20 m (arising due to shifts in the input data and interpretative errors), which typically corresponds to half a seismic wavelength in the interval of interest.

Interpretational framework for sill intrusions

The sills were interpreted starting from an extensive analysis of all the available well data and a compilation of all the wells with a definitive intersection with dolerite intrusions (Table 1). The acoustic diagnostic features of the sills, such as polarity and seismic character, at the intersection with each calibration well were then extrapolated to the surrounding areas. Regional mapping of the sills focused on an area bordering the trajectory of the central dyke group (Fig. 1a).

Standard well-to-seismic ties (cf. White and Simm 2003) were not possible due to the paucity of density logs acquired across the Zechstein Group. This meant that the generation of synthetic seismograms was impractical because it would rely solely on sonic logs. The calibration techniques and uncertainties are outlined in detail in the Results section. All 15 calibration wells were tied to the 3D seismic volume using check-shot data derived from vertical seismic profiling. The clear intersection with sills and the presence of thick salt layers resulted in an excellent calibration of the seismic data with an uncertainty of just a few metres for the upper and lower contacts of the sills.

We identified five wells where the operator's interpretation of the lithology changed from sedimentary to igneous following additional studies of cuttings samples, such as measurements of the magnetic susceptibility. These cases of misinterpretation were cross-checked with the seismic characteristics of the suspect interval for comparison with those wells where unambiguous igneous lithologies were calibrated with the seismic data.

Results

Interpretation of sill intrusions using well data

Igneous intrusions were identified in 15 wells in the study area covering Quadrants 43 and 44 of the UK Sector of the South Permian Basin using a combination of the lithology of cuttings samples and petrophysical measurements from downhole logging operations (Fig. 3) (Table 1). The intrusions were almost exclusively found within the upper part of the Zechstein Group, close to the boundary between the Z3 and Z4 cycles. The composition of the igneous rocks is typical of dolerites, but with considerable variations in texture and grain size (Table 1). Only one small core sample is known to have been obtained during a fishing trip to clean the bottom hole of well 44/24b-2A. None of these igneous bodies has been dated radiometrically. A further 44 wells in the study area were documented as having no evidence of igneous material within the Mesozoic section (Table 1). These wells provided information on the variation in the stratigraphic succession of the Zechstein Group in the region containing the sills and provided a template for comparison with the local evaporite stratigraphy in wells where intrusions were present.

The 15 wells proving intrusions are clustered over *c.* 60 km in Quadrant 44 (Fig. 3). However, this does not imply a restricted occurrence of the dolerite intrusions, more a reflection of the incomplete sampling by wells. Significantly, the locations of these 15 wells are generally all within 5 km laterally from the dykes belonging to the MDS, as mapped by Carver *et al.* (2023) (Fig. 3).

Only one previously published study documents dolerite intrusions within the Zechstein Group in this area of the Southern Permian Basin (Gauer *et al.* 2004). However, the unpublished completion reports for most of the 15 calibration wells all interpret these intrusions as either dykes or sills or as undifferentiated igneous rocks (Table 1). Gauer *et al.* (2004) interpreted sill intrusions in three wells (44/24-2, 44/24-4 and 44/24-5), observing that they intruded at a specific level within the Zechstein Group where potassium-rich salts are well developed in the uppermost Z3 cycle (Fig. 4).

The stratigraphic position of the main intrusions in all 15 wells is exclusively within the uppermost Z3 cycle, either at or immediately below the important marker unit of the Roter Salzton (Fig. 4) and clearly above the regionally important Hauptanhydrit marker unit (the informally termed ‘stringer’ of Strozyk *et al.* (2012), a combination of thin basal claystone, thin dolomite and thicker anhydrite layers). In some wells, the Roter Salzton is completely missing (e.g. well 44/23b-11), in which case placing the precise position of the intrusion is uncertain. However, where the Roter Salzton is present as a reference datum for the intrusion level, the host stratigraphy is notable for the almost complete absence of the potash-bearing unit of the uppermost Z3 cycle (Z3K) that is widely developed at this position across the basin (Smith and Crosby 1979; Smith *et al.* 2014) (Fig. 4).

By contrast, potassium salts are found to occur within all 44 wells in the study area that do not intersect igneous intrusions within the laterally correlative uppermost Z3 cycle. Using the gamma ray calibration method devised by Kemp *et al.* (2016), it can be estimated that the potash units of the local basinal context comprise a net 10–20% by volume of the typically 60–80 m thick potash-bearing interval, along with the more predominant occurrence of Z3 halite. This is exemplified in a representative correlation between a neighbouring sill–no sill well pair, where the typical ‘background’ Z3K unit is seen to be 65 m thick in well 44/18-3, but absent from the interval beneath the sill in well 44/23g-14 (Fig. 5).

Well-to-well correlation between wells calibrating the sill intrusions to their nearest neighbour wells with no intrusion revealed several interesting relationships (Fig. 6). First, for all the wells with sills, it was found that the Z4 cycle is generally thinner than in the non-sill wells. Second, there is considerable overlap in Z4 cycle thicknesses between the two groups of wells, but there is a shift to greater thicknesses for non-sill wells by *c.* 10 m in the median value. Third, for the sill calibration wells, the combined thickness of the sills and the Z4 cycle exceeds the thickness range for the Z4 cycle in the non-sill wells by *c.* 45 m.

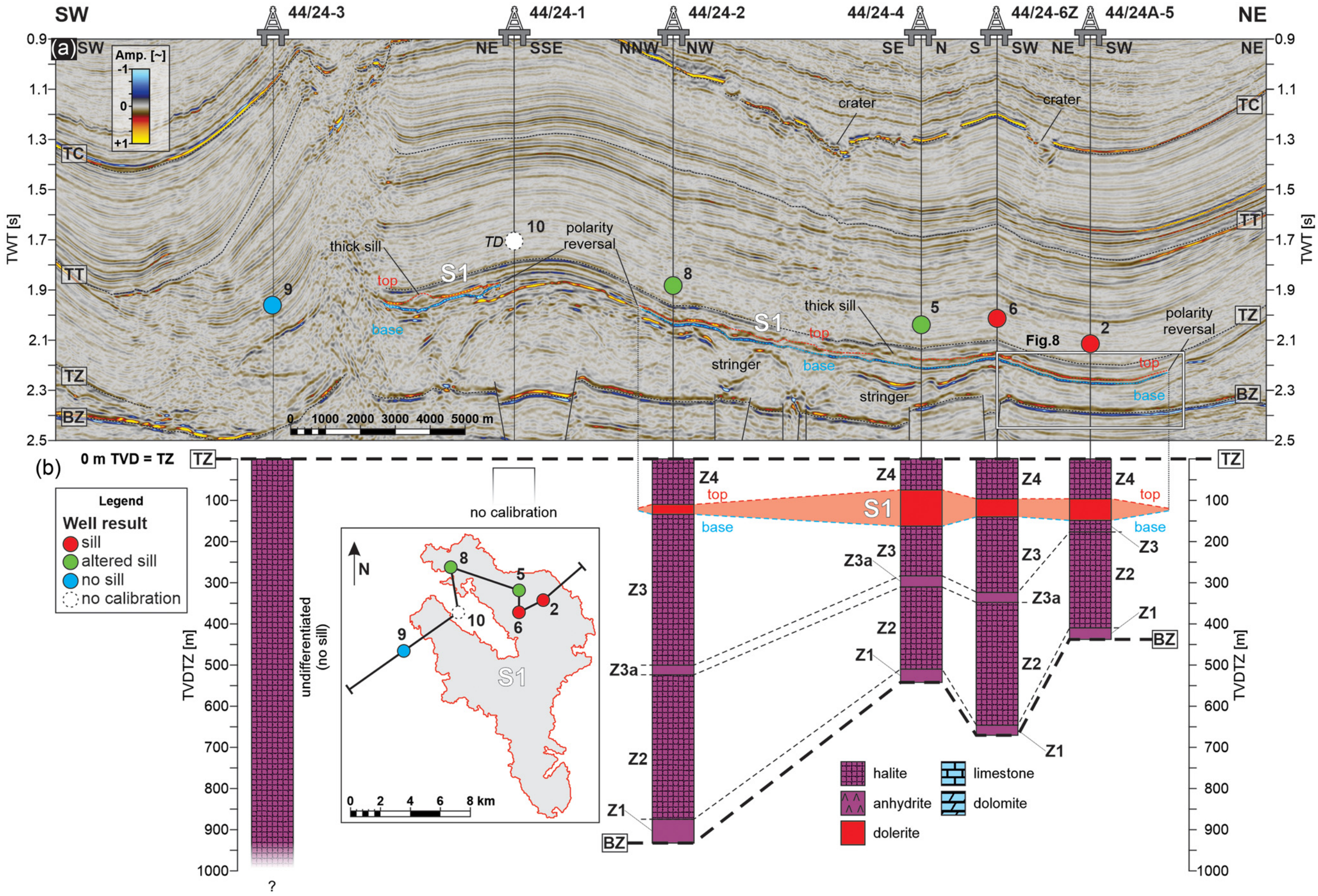

Fig. 4. (**a**) A well-to-seismic tie arbitrary line profile for a well correlation panel across the study area (location in Fig. 3) showing the general stratigraphy into which the Early Cenozoic dykes and sills were intruded (data truncated at 0.9 s TWT). Wells are indicated by colour coding corresponding to the legend in Figure 3. The top and base sill reflections are indicated in red and blue, respectively. The indicative positions of dykes are based on the interpretation of seismic disturbance zones. Note that the sills are strikingly concordant with the uppermost Zechstein Group. (**b**) Well correlation panel for Zechstein Group (inset gives location) with the main cycles indicated and the datum placed at the Top Zechstein. The variable thickness of sill S1 shown as is the stratigraphic level of intrusion into the uppermost Z3 cycle. TC, Top Chalk; BCU, Base Cretaceous Unconformity; TT, Top Triassic; TZ, Top Zechstein; BZ, Base Zechstein.

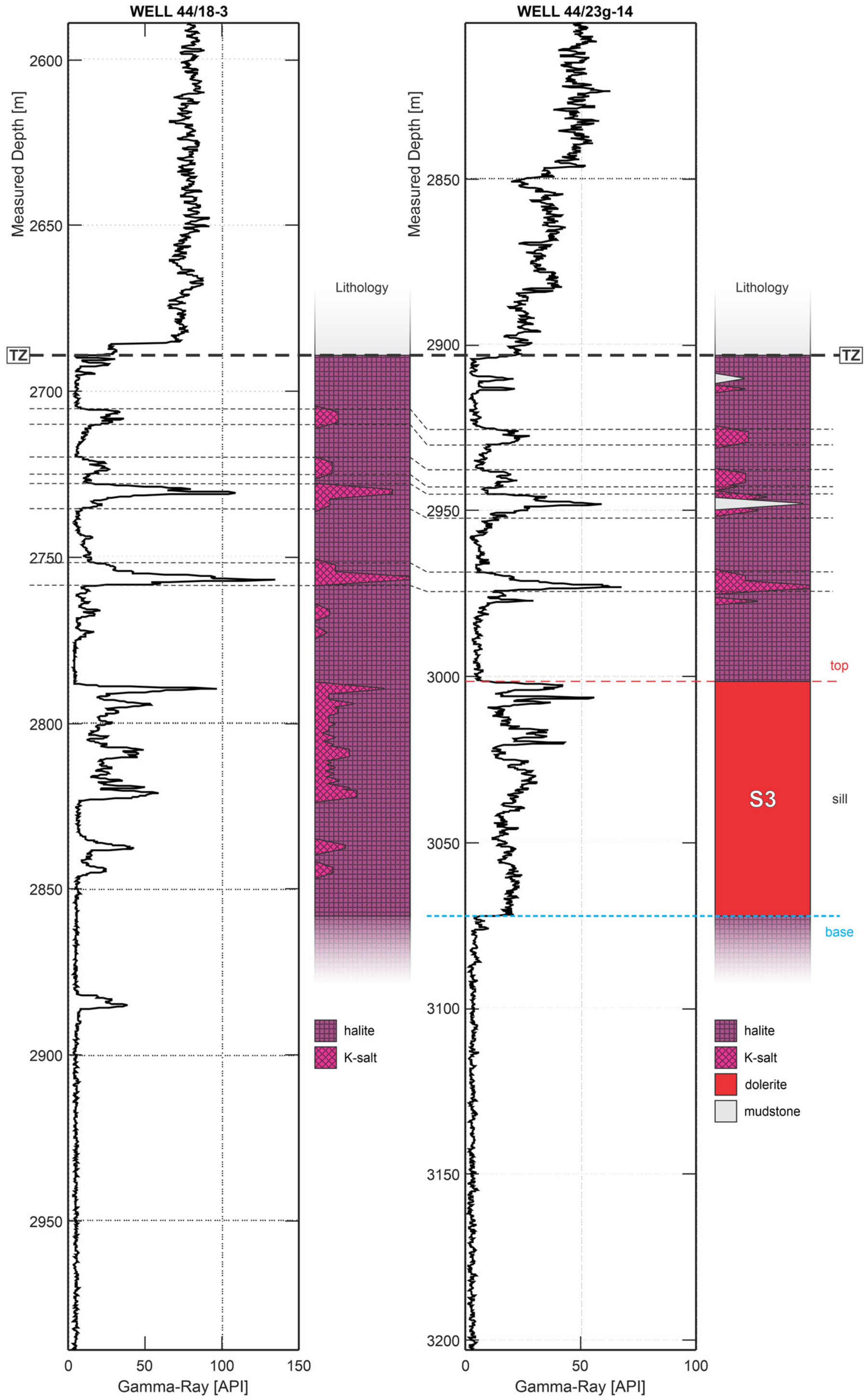

Fig. 5. Well correlation between two wells with and without a sill intruded at the upper Z3 cycle. The displays are gamma ray values (API units), with low values indicating halite and higher values generally corresponding to potash salts or to dolerite. The proportions of halite and potash salts are schematic, based partly on the methodology in Kemp *et al.* (2016). Well locations in Figure 3; Z1, Z2, Z3 and Z4 refer to Zechstein cycle numbers. The potash salts in the Z4 cycle are excellent correlation markers for this well pair, but this belies the variability in potash distribution in both the Z3 and Z4 cycles more generally. If this correlation is taken as a reference, then sill S3 has intruded at the Z3–Z4 boundary and corresponds to the removal of the potash-bearing interval of the upper Z3 (Z3K). TZ, Top Zechstein.

In addition to the 15 well intersections of intrusions at the Z3–Z4 boundary, an 11 m thick dolerite intrusion of unknown type was intersected within the Silver Pit Formation (Rotliegend) of well 44/24b-A4 and a dyke was intersected in the Triassic section in well 44/24-4z (Fig. 7). This latter intersection of a dyke by a deviated well occurs in the axis of an SDZ associated with dyke B of the central dyke group mapped by Carver *et al.* (2023). This intersection with this 5 m wide dyke in precisely the seismically predicted position is important in that it validates the previously argued interpretation that the SDZs represent broader zones of seismic artefacts associated with the much thinner dykes (cf. Underhill 2009; Wall *et al.* 2010). A similar validation of dyke interpretation from an SDZ using well data was demonstrated by Magee and Jackson (2020) for their analysis of a dyke swarm in NW Australia.

Descriptions of the intrusive rocks

Borehole cuttings of the intrusive rocks are generally described as hard angular fragments of dolerite, occasionally with conchoidal fractured surfaces, light grey, brown, purple to black in colour, and crystalline to glassy in appearance, occasionally speckled with millimetre-scale plagioclase laths and lightish to green acicular crystals (Fig. 8). Vein quartz is associated with the dolerite in some wells. Different degrees of alteration are mentioned in some wells, with a white/pink/pale green appearance to the cuttings and the presence of calcite. The dolerite is occasionally noted as containing some anhydrite, claystone or halite ‘inclusions’ (Fig. 8).

A detailed petrographic study was undertaken by the well operator on cuttings from the intrusion intersected in well 44/24a-5

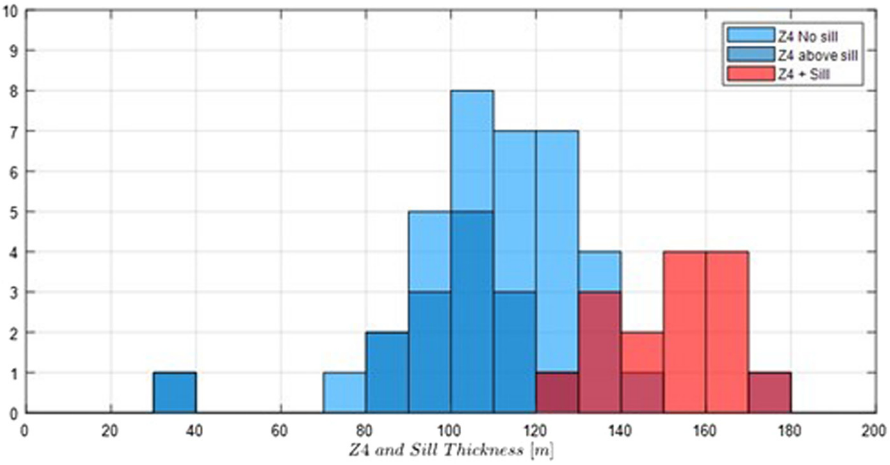

Fig. 6. Histogram of thicknesses of the Z4 cycle in 22 wells in which there is no sill intersected (labelled Z4 No sill) and 15 wells with sill intrusions (labelled Z4 above sill). Where sills are present, the Z4 thickness tends to be tens of metres thinner than where they are absent. Also shown is the combined thickness of sills plus Z4 (labelled Z4 + Sill). These latter values are skewed to the right, indicating that where sills are intruded the full thickness is not compensated for by loss of thickness of the overlying Z4 cycle sediments.

(Fig. 8) (NSTA Archive). This revealed three main lithologies: basaltic glass, coarsely crystalline equigranular basalt and porphyritic basalt. The variation between these lithologies was based on the dominant size ranges of phenocrysts of plagioclase and olivine and the groundmass characteristics. The larger plagioclase laths are up to 0.5 mm in size and show twinning with minor alteration haloes. However, the lithological relationships could not be determined (e.g. layered or chaotic) due to the mixing of cuttings during transport to the surface.

On wireline logs, the intrusions can be differentiated from their host evaporite lithologies by their higher gamma ray values and more erratic resistivity signatures (Gauer *et al.* 2004) (Figs 5, 8). Sonic and density logs are rarely obtained over this interval; however, the rate of penetration log, expressed in minutes of drilling time per metre of drilling distance (depth), generally shows a remarkable increase from 2–4 min m^{-1} through non-anhydritic evaporites to >24–120 min m^{-1} across the intrusions.

In 12 of the 15 calibration wells, dolerite is directly juxtaposed with halite of the Z3 cycle at the lower contacts of the intrusions and with probable halite of the Z4 cycle at the upper contact. Well 44/24b-A4 is an exception, with dolerite juxtaposed against tens of metres of claystone at both contacts. This is highly anomalous from

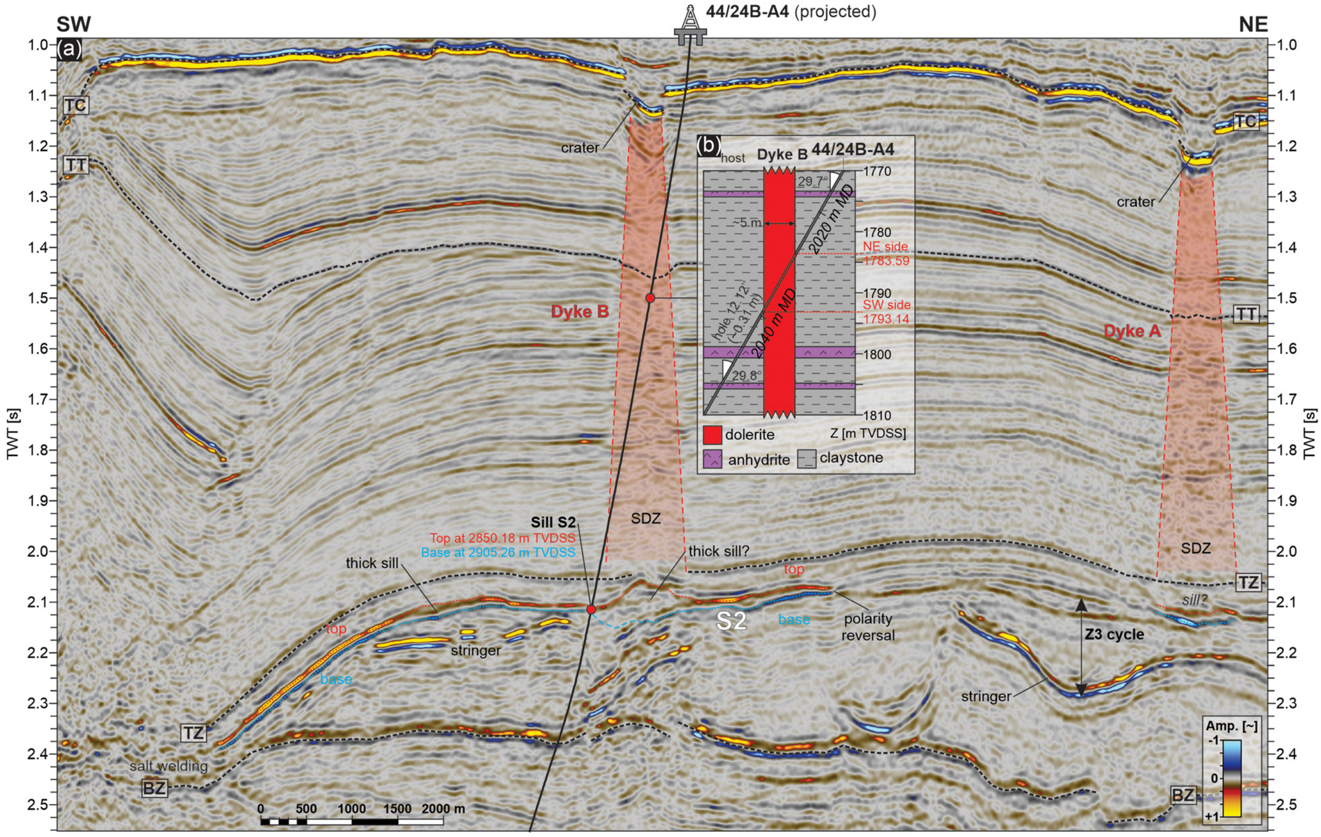

Fig. 7. Seismic calibration of well 44/24B-A4. (**a**) Seismic profile along the well trajectory (deviated) showing the intersection with dyke B hosted at the intersection position within Triassic mudstones and located precisely midway across the seismic disturbance zone associated with the dyke (red shading) and vertically beneath the deepest part of the crater in the Chalk. The well calibrates sill S2 (55 m thick at this location) and a high-amplitude top and base sill reflection pair that exhibits a clear polarity reversal and sharp amplitude cut-off on its NE margin. Sill S2 plunges down-dip into a major salt structure that evidently grew during the Mesozoic prior to sill intrusion. The thicker sill portion indicated beneath dyke B may be perturbed by artefacts relating to the dyke. (**b**) Inset cross-section in true depth scale showing the geometry of the dyke intersection. This shows that the dyke is *c.* 5 m thick at this stratigraphic position, but may be thicker at depth. TC, Top Chalk; TT, Top Triassic; TZ, Top Zechstein; BZ, Base Zechstein; SDZ, seismic disturbance zone.

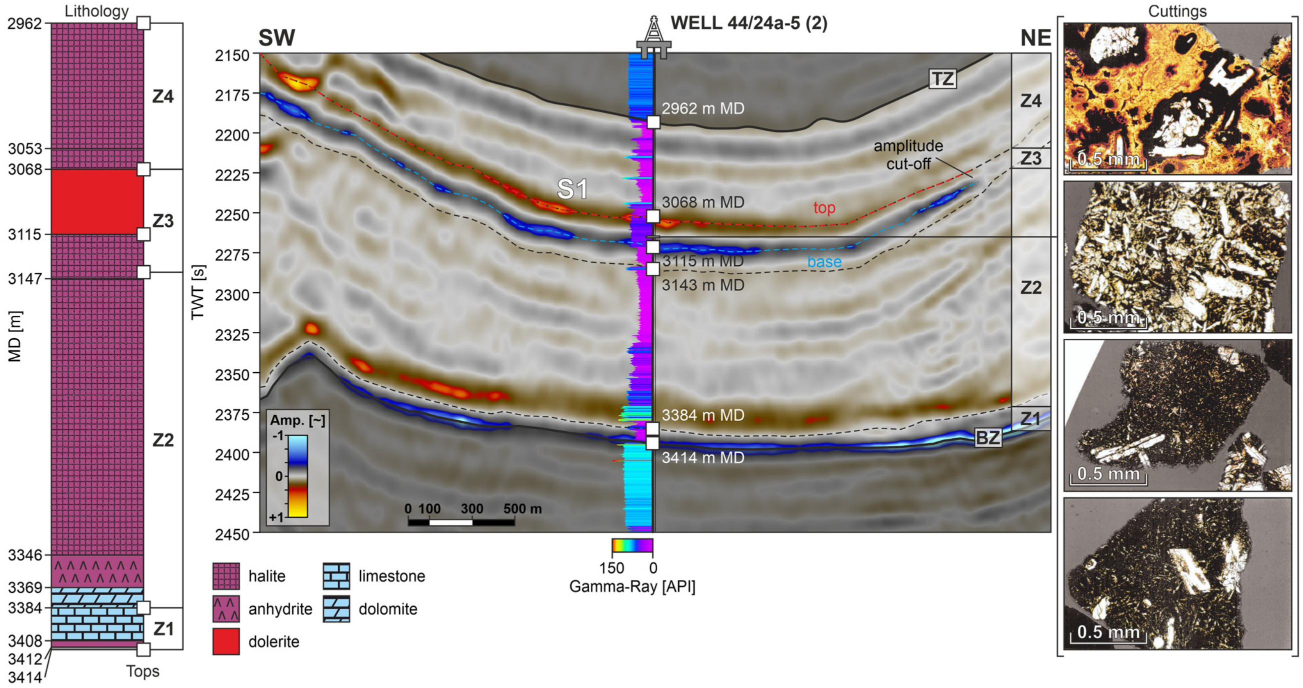

Fig. 8. Well-to-seismic tie for well 44/24a-5 showing the detailed tie for sill S1 intruded within the Zechstein Group. The gamma ray log is tied using the vertical seismic profile computed by the well operator (see NSTA archive for source details). The top and base sill reflections tie to the upper and lower sill contacts in the well. The depth values and generalized lithology derived from the well completion reports is shown in the left-hand panel and a series of thin sections showing the textural variation in the dolerite is shown in the right-hand panel (see text for details).

a stratigraphic perspective because such thick claystone intervals are not seen in any of the neighbouring wells in this stratigraphic position. Claystone inclusions up to 2 m thick within the dolerite have been described from several wells and may be xenoliths or broken bridges comparable with those commonly described from outcropping sills (e.g. Thomson and Hutton 2004). Halite inclusions of a sufficient scale to be identified in cuttings and logs are only found in one well (44/11-3). If this is a xenolith, then it demonstrates that cooling was sufficiently rapid so as not to lead to complete assimilation.

Contacts are more commonly sharp than gradational. Petrophysical logs show an abrupt boundary with the host evaporites in the majority of cases, but in some wells an irregular log motif at the contact is suggestive of some degree of interleaving of dolerite and host (e.g. well 44/23g-14). Intrusive margins are commonly altered. Dark grey claystone and dolomite are often reported for cuttings from the contact region.

No dip-meter log is available for any of the 15 wells, meaning that the contact geometry is uncertain. The thickness of the intrusions ranges from 20 to 98 m (Table 1). The 15 wells are a mixture of vertical and deviated trajectories, so this range of thickness values is consistent with the sub-horizontal to modestly dipping contacts typical of sills. Dyke thicknesses rarely exceed 20 m when measured at outcrop in northern England closer to their source in Mull (Land 1974). Reports of dyke intrusions in some of the well completion reports are therefore most probably erroneous and this interpretation of gentler dipping contacts is fully substantiated by the geophysical interpretation. An exception is the dyke intersected in well 44/24-4z (Fig. 7).

Hydrothermal alteration is widely reported in descriptions of cuttings from many of the 15 sill calibration wells. This probably explains several cases where dolerite was initially misidentified as dolomite, anhydrite or dark grey claystone, but subsequently found to have a high magnetic susceptibility and re-interpreted as either volcanic or intrusive (e.g. wells 44/23-11 and 44/23-13; Table 1). It is notable that these misidentified intervals are at a similar stratigraphic position and have similar thicknesses to the positively identified dolerite intrusions. Hydrothermal alteration to a whitish colour is often reported onshore in the Northumberland coalfield (Land 1974) and includes the formation of carbonate alteration products. Cuttings samples of altered dolerite could therefore easily be mistaken for dolomite or anhydrite. Wells with alteration of the main intrusive body are distinguished from those with an alteration halo, where likely alteration products are interpreted only in the contact region (Fig. 3; Table 1).

Seismic characterization of the intrusive complex

The overwhelming evidence provided by the well data is that dolerite sills intruded at roughly the level of the uppermost Z3 cycle at some time after the deposition of the Late Permian evaporite sequence. The well data also provide some evidence of alteration of the primary igneous compositions. However, given the limited sampling of the well distribution, it is not possible to define the intrusive geometry with the well data alone, nor the distribution of intrusions in the wider basinal context. The clustering of wells calibrating the intrusions within *c.* 5 km of dykes from the MDS provides a first-order guide to seismic mapping of the sills and these wells also crucially provide a means to tie the lithologies to the seismic data through multiple well-to-seismic calibrations.

Acoustic expression of sill intrusions in the study area

The wedge model presented in Figure 2 clearly shows that the top of a sill at a halite–dolerite contact is marked by a positive amplitude reflection representing a substantial increase in acoustic impedance (Fig. 2). The dolerite–halite contact at the base of the sill is marked by a negative amplitude reflection. As is typical in wedge models of sills embedded in lower acoustic impedance materials (e.g. Smallwood and Maresh 2002), the amplitude response of both the upper and lower contacts reaches a maximum value at the tuning thickness. For parameters representative of our study area, this peak amplitude occurs when the sill thickness reaches 55–60 m (Fig. 2). Sills thinner or thicker than this value therefore exhibit reduced amplitude reflections.

The top sill reflection in the study area is consistently characterized by a moderate- to high-amplitude response (Figs 4, 8 and 9). Lateral amplitude variation is typically characterized by intermittent segments of amplification and dimming on variable length scales across the sills. This variation makes lateral correlation challenging in places, but, in general, the sills were easily identified from the background seismic response of the Zechstein Group simply because the sills exhibit a generally close-to-tuned response over much of their surface area. This is exemplified by the well-to-seismic tie of well 44/24-5a (Fig. 8) and by the ease of seismic correlation between calibration wells (Fig. 9).

The base sill reflection is consistently negative in amplitude across the study area and is often amplified, but it shows intermittent dimming similar to that of the top sill reflection. At the lateral tips, the base sill is often amplified, producing a clearly identifiable amplified pair with the top reflection (Fig. 9). However, the amplification of the base sill is not always consistent with that of the top sill. Over most of the mapped area, the small separation of the top and base sills is such that no internal reflectivity can be observed (Figs 8, 9).

Amplifications of top and base sill reflections are often observed towards the tip of the sills, but this is not consistent over the mapped intrusions. Conversely, dimming is often observed in thick sill regions where the amplitude rapidly changes with increasing separation between the top and base reflections (Figs 4, 8 and 9).

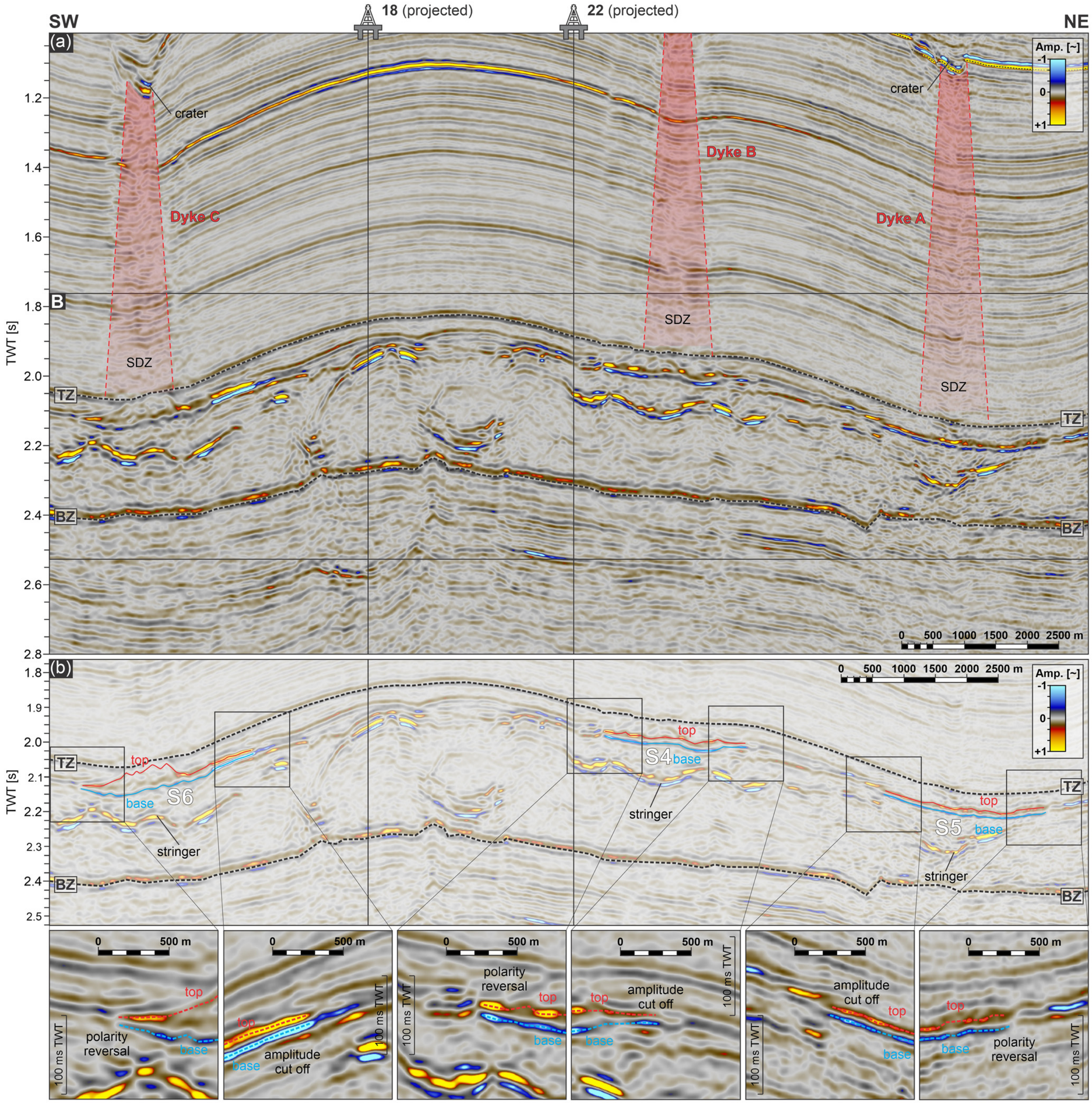

Fig. 9. (**a**) Seismic profile (truncated above 1.0 s TWT) close to two wells showing the seismic expression of sills S4, 5 and 6 in relation to the seismic disturbance zones of dykes A, B and C. Note the concordant geometry of the three sills with respect to the uppermost Zechstein Group. (**b**) Zoomed inset panels showing the acoustic response to the lateral termination of the three sills, characterized by amplitude cut-offs either with or without polarity reversals. TZ, Top Zechstein; BZ, Base Zechstein; SDZ, seismic disturbance zone.

Dimming is systematically observed in relation to the SDZs associated with the dykes (Carver *et al.* 2023; Pryce *et al.* 2025) (Fig. 9). These regions are characterized by poor reflection continuity and amplitude variation and the interpretation of the top and base sill reflections within the footprint of the SDZs is uncertain due to the scattering and attenuation linked to dyke intrusions.

The lateral margins of the sills are easily recognizable by the generally sharp amplitude cut-offs of both top and base sill reflections combined with an increase in amplitude on both the top and base reflections as the margin is approached (Fig 9). Two different modes of amplitude cut-off occur: (1) where the amplitude simply reduces to the background reflectivity with no polarity reversal; and (2) an equally abrupt reduction in amplitude, but with polarity reversal (Fig. 9). These are interpreted in more detail in the following sections.

Sill mapping overview

The mapped sills are distributed for >130 km and closely cluster along the strike of the MDS, crossing Quads 43 and 44 of the UK Sector (Figs 1, 3 and 10). All the sills are transected along their lengths by constituent dykes from the central dyke group of the swarm. The dyke traces are not symmetrically disposed with respect to the sills, but crudely bisect individual sills. Opposing perimeters are not equidistant from any given bisecting dyke. No dolerite intrusion has been calibrated by any of the >300 wells in the UK Sector of the Southern North Sea outside a corridor that is defined by the positions of the individual dykes of the MDS (Table 1). The specific relationship between the sills and coincident dykes is obscured by the seismic artefacts related to the dykes, so it is not possible to say from direct seismic imaging whether the sills cross-cut the dykes or vice versa.

The outline map of the sills presented in Figure 3 is shown as a peak amplitude display of the base sill reflection in Figure 10. Individual sills are defined as such when their perimeter closes and forms a discrete entity with markedly higher amplitude values than the laterally contiguous reflectivity (Fig. 9). In total, six separate sills (S1–S6) (Fig. 3) have been mapped in the primary study area, four of which are calibrated by wells; the remaining two are based entirely on the seismic characteristics mapped by extrapolation from neighbouring calibrated sills. In addition, several possible sills (uncalibrated) with smaller areas and narrower widths than sills S1–S6 have been mapped along the dyke trends some tens of kilometres to the WNW and ESE of the primary study area (Fig. 1), but their amplitude response is so severely affected by the SDZs that they were not included in the detailed amplitude mapping (Fig. 10). The closely clustered group of the sills extends for >100 km along the corridor defined by the central group of the MDS and they are all contained within the 3D MegaSurvey area – that is, the seismic data allowed the mapping of their full extent within the study area.

The stratigraphic position of the sills as interpreted on the seismic data shows a remarkably concordant geometry over the entire area of each individual sill (Figs 4, 8 and 9). There is no evidence of any transgressive geometry at the scale of vertical seismic resolution. The reflection geometry of the host interval sometimes shows localized deformation in response to sill intrusion in the form of low-relief folding of the Z4 cycle (Fig. 9), but this is barely discernible above the limit of vertical seismic resolution and cannot be mapped systematically around the sill margins. The Top Zechstein reflection is itself folded and faulted concordantly with the underlying Z4 cycle. This deformation is the cumulative effect of regional-scale salt tectonics during the later Mesozoic and Cenozoic (Stewart and Coward 1995). Remarkably, where there is significant dip on the Z3–Z4 boundary due to halokinesis, the sills maintain their concordant geometry irrespective of the deformation.

The planforms of the individual sills form two distinct groups. The first consists of narrow sills (S3–S6) with smaller width to length ratios, elongated in a WNW–ESE direction along specific dykes and with a mean distance from the feeder dyke to the sill perimeter of 1.35 km ($N = 108$). The second group consists of more elliptical sills (S1 and S2) with larger width to length ratios, a general NNW–SSE long axis orientation and a mean distance to the nearest feeder dyke of 2.65 km ($N = 56$) (Fig. 10). In the second group, the planform relationship of the sill margins points to a feeder relationship from more than one dyke, whereas individual sills in the elongate group can be interpreted as having been fed from a single dyke.

In addition to the contrast in planform between the two groups, there is also a contrast in their structural context. The elongate sills have been folded concordantly with large wavelength, WNW–ESE-striking salt-cored buckle folds that post-date the sill intrusion event in the Late Paleocene (Wall *et al.* 2010). These large buckle folds have synkinematic growth packages dated from the Eocene to Mid-Miocene (Hughes and Davison 1993; Stewart and Coward 1995). The NNW-trending elliptical sills (S1 and S2, Fig. 10) are aligned along a major synclinal structure adjacent to a prominent salt wall that is clearly seen on the regional Top Chalk map (Fig. 1). This salt wall evidently grew much earlier, in the later Mesozoic (Jenyon 1988; Stewart and Coward 1995), so was already responsible for considerable deformation of the Zechstein Group at the time of intrusion in the Late Paleocene (Wall *et al.* 2010). The NNW elliptical axes thus exhibit a form of structural control interfering with the dyke-fed locus, whereas the elongate group is not influenced by structure. These relationships are expressed on the map of sill perimeter types in Figure 10b.

The detailed geometry of the individual sill perimeters varies considerably and at contrasting length scales, although not all this variation may be due to the geology, particularly at the smaller length scales. The sill perimeters were mapped based on the sharp amplitude cut-offs with or without polarity reversals noted earlier (e.g. Fig. 9). However, close inspection of the amplitude variation towards the perimeters shows that the amplitude decay occurs over a finite lateral distance (Fig. 11). Measurements of this ‘decay’ distance are of the order of 100–200 m along the well-imaged portions of the sill perimeters. This is roughly five to ten times the bin size of the 3D seismic volume and hence exceeds the lateral resolution by some margin (Brown 2011). The observed systematic reduction in amplitude is consistent with a gradual tapering of sill thickness towards the actual lateral tip of each sill, but the precise shape of the tip is not seismically resolvable. Small-scale irregularities in the perimeter geometry >100 m in dimension therefore probably represent true localized variations in thickness in the region approaching the true tip position.

Larger scale irregularities of the sill perimeters expressed as pronounced salients and re-entrants are particularly apparent for the elongate group of sills, best exemplified on sill S6 (Fig. 10d). These salients are >1 km across and protrude into the host for 1–2 km beyond the general outline of the perimeter.

Interpretation of amplitude maps

Previous studies have made the important point that seismic amplitudes cannot be easily interpreted as a proxy for the thickness of sills when the typical range of sill thickness falls within the uncertainty range of the tuning thickness (Berndt *et al.* 2000; Smallwood and Maresh 2002). The amplitude could be influenced by several factors other than variations in thickness. These include: (1) internal compositional variation in the sills; (2) impedance contrast with the underlying evaporite units; (3) dimming associated with an increase in thickness and intersection with dykes (amplitude shadow); and (4) the dip of the intrusion.

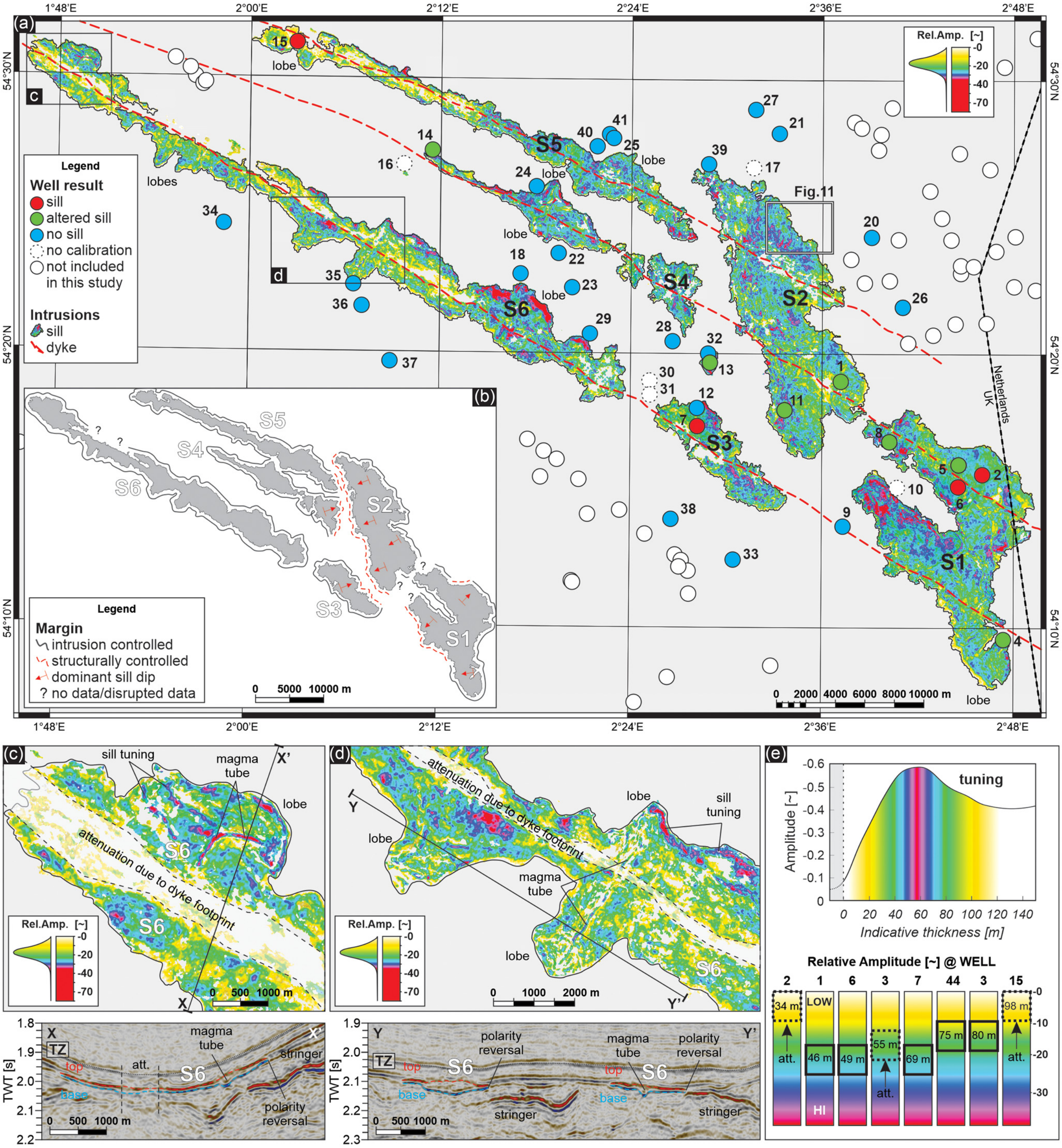

Fig. 10. (**a**) Peak amplitude map of the base sill horizon for sills S1–S6. Reference well locations are shown (see also Table 1 and Fig. 3). Amplitude values are dimensionless negative values. (**b**) Perimeter classification map for sills S1–S6, with categories reflecting data quality and whether or not the sill margins were structurally controlled. The main perimeters with a strong structural control are those bordering the NNW–SSE-trending salt structure (see Figs 1, 4). The 'stringer' corresponds to a high-amplitude reflection produced by an anhydrite layer near the base of the Z3 cycle. (**c**, **d**) Details of the amplitude map across the sectors of sill S6 that have a pronounced salient along their perimeter. These two maps show the internal variations and positions of curvilinear anomalies interpreted as magma tubes. The seismic profiles across these amplitude anomalies show that they are narrow regions of sill thickening with a channel-like profile. (**e**) Amplitude as a function of sill thickness, assuming the classical wedge model of Figure 2 and showing the tuning thickness at 55–60 m. For comparison, the relative amplitude values measured at well intersection positions for the base sill reflection in part (a) are shown for eight of the calibration wells intersecting the sills. These show that measured thicknesses correspond well to amplitude values predicted from the wedge model. Note that similar amplitude values can correspond to very different thicknesses – for example, wells 2 and 15 have similar amplitude values, but differ in thickness by 64 m.

To evaluate the possible variation in thickness in the mapped sills, we extracted the peak amplitude value of the base sill (Fig. 10). The amplitude variation for the six sills is characterized by a patchy character for each individual sill, which likely results from a combination of thickness variation and the additional complicating factors noted earlier. The relative amplitude values are generally dominated by an acoustic amplitude of *c.* 20–30 relative amplitude units, with localized patches with a lower amplitude range of 10–15 units or a higher range of >30 units. These patches are irregularly distributed and are typically >500 m in lateral extent and are

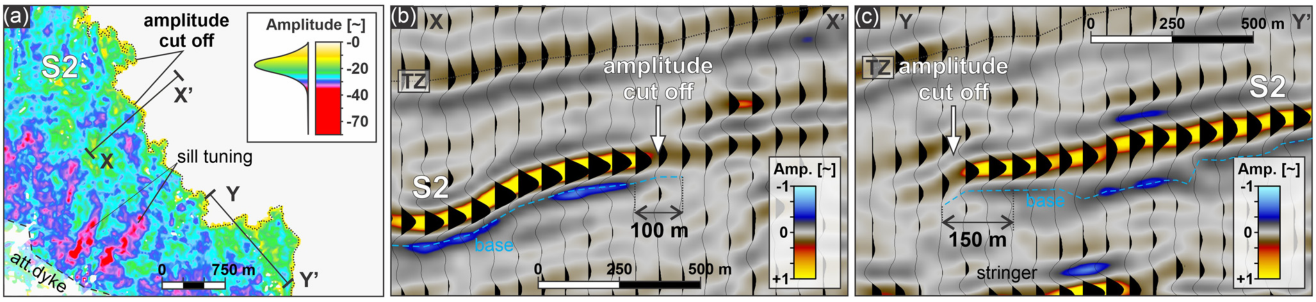

Fig. 11. Amplitude variation close to the lateral tips of the sills. (**a**) Portion of the peak amplitude map of sill S2 showing the amplitude variation on the base sill towards the northeastern margin of the sill (relative amplitude scale corresponds to that on Fig. 10). The irregular perimeter is mapped at the sharp amplitude cut-off. (**b**, **c**) Two seismic profiles shown in a wiggle peak/dual polarity display to highlight the lateral reduction in amplitude of both the top and base sill reflections within 100–150 m of the amplitude cut-off position. This zone of reducing amplitude probably corresponds to a tapering sill thickness towards the physical tip, but the precise position of the tip cannot be located more accurately. Profiles located in part (a). The stringer corresponds to a high-amplitude reflection produced by an anhydrite layer near the base of the Z3 cycle. TZ, Top Zechstein.

therefore spatially resolved. There does not appear to be any clear kinematic indicator (such as ridges, internal lobe-to-lobe contacts or steps) similar to those reported elsewhere (Thomson and Hutton 2004; Trude 2004; Hansen and Cartwright 2006; Thomson 2007; Magee *et al.* 2016; Köpping *et al.* 2022).

However, several curvilinear higher amplitude anomalies are found distributed close to the sill margins where the perimeter takes the form of a salient. Seismic profiles across the amplitude anomalies for sill S6 show that the amplitude anomaly corresponds to an increase in thickness where the base sill reflection forms a narrow, linear depression, but the sill top is concordant (Fig. 10c, d). Miles and Cartwright (2010) reported similar amplitude anomalies from sills intruded into claystones along the Norwegian margin and interpreted them as magma tubes (conduits for preferential magma flow) that acted to channel the flow into the sill lobes. From the relationships seen between the salient and the amplitude anomalies for sill S6, it is interpreted that some form of magma tube or channelized flow conduit developed during sill emplacement and the preferential flow localization allowed the development of the lobate perimeter geometry. Similar flow localization has been reported for sills at outcrop (Holness and Humphreys 2003) and on seismic data (Thomson and Hutton 2004; Hansen and Cartwright 2006; Köpping *et al.* 2022).

The amplitude response of the base sill reflection was calibrated with the thickness of the sills at the calibration wells (Fig. 10e). This calibration shows that, for a tuning thickness of 55–60 m (Figs 2, 10), values <30 relative amplitude units can be associated either with sub-tuning thicknesses ranging from *c.* 10 to 45 m or with supra-tuning thicknesses of 65–100 m. Similar amplitude values could therefore hide a potential four-fold variation in thickness. The amplitude response could indicate: (1) true thinning towards the margins of the sills, observed, for instance, along the NE margin of sill S6, the NE margin of the southern branch of sill S1 or on the NE margin of sill S4 (around well 24, Fig. 10a); (2) areas of thin sills, observed with a patchy character, such as the north portion of sill S2 (Fig. 10a); and (3) association with internal features with abrupt variations in thickness, such as the magma tubes.

Sill volumetrics

This calibration exercise fully confirms the caution advised in previous studies about over-interpreting the thickness or internal structure of sills from the amplitude response of sills close to the tuning thickness. Based on this uncertainty, any attempt at calculating sill volumes using isopach maps would be impractical.

To estimate the volumes of individual sills, we therefore defined a probability distribution function based on the mean and standard deviation of the sill thicknesses measured in the 15 calibrated wells (Table 1). We then approximated the sill geometry as tabular sheets with rectangular lateral tips and computed the volume using a Monte Carlo framework with a sample size $N = 1 \times 10^4$.

Based on these assumptions and framework, and using the areas calculated from the mapped outlines of sills S1–S6, the total combined volume of the six sills is estimated to range between 19.4 and 26.2 km^3 (P25 and P75 values, Table 2). Individual volumes exhibit similar percentile ranges – for example, sill S1 ranges from 4.66 to 6.31 km^3 at the P25 and P75 values, respectively. We consider that the ranges in the Monte Carlo simulations of the estimated volumes are a reasonable reflection of the uncertainties inherent in limited well samples and vertical seismic resolution limitations. For comparison, the combined volume of the central dyke group over its total length was estimated as *c.* 200 km^3 (Carver *et al.* 2023).

Discussion

The observations from the well and seismic data presented in the preceding sections point conclusively to the emplacement of a major dolerite sill complex intimately connected to and fed from the major dykes of the central group of the MDS at the distal limit of their long-range dyke propagation *c.* 600 km from their source on Mull. The localization of all the sills to within 5 km of mapped dyke traces makes any other option for feeding the sills highly improbable. We name this clustered group of sills the Dogger Sill Complex after its geographical position in the Southern North Sea.

Given that this volumetrically significant sill complex was fed by dykes of the MDS, it is pertinent to ask what impact, if any, the intrusion of this sill complex may have had on the propagation history of this giant dyke swarm. In addition, perhaps the most

Table 2. Areas and volumes for sill S1 to S6

			Volume (km^3)		
Sill	Area (m^2)	Area (km^2)	P25	P50	P75
S1	1.03×10^8	1.03×10^2	4.66	5.46	6.31
S2	99 775 000	9.98×10^1	4.51	5.29	6.11
S3	24 752 500	2.48×10^1	1.12	1.31	1.52
S4	52 965 000	5.30×10^1	2.39	2.81	3.24
S5	33 108 750	3.31×10^1	1.50	1.76	2.03
S6	1.15×10^8	1.15×10^2	5.20	6.10	7.04
Total		4.29×10^2	19.4	22.7	26.2

Volumes are based on a tabular sill geometry with the thickness values determined statistically from the calibrated values reported in Table 1, specifically the P25, P50 and P75 of the sill thickness distribution.

striking aspect of the emplacement of the sills is their concordant sheet geometry, almost exclusively intruded at a narrow stratigraphic interval coinciding with a potash-rich interval of the Z3 cycle (Z3K; Fig. 5). This concordance, irrespective of the host geometry (dipping v. sub-horizontal stratal geometry) implies that there must have been something specific about the Z3K interval that greatly facilitated sill intrusion. These two thematic questions are discussed in the following sections, beginning with the broader context of sill intrusion into evaporite sequences.

Sill intrusion into evaporite sequences

Although there are many documented examples of sill complexes imaged using 3D seismic data (e.g. Magee *et al.* 2016, 2019; Köpping *et al.* 2022), the vast majority of these have featured sills that intruded into clastic sedimentary successions. Only a single previous study has interpreted seismic data to show sills intruded into an evaporite sequence: in the Santos Basin, Brazil, where Magee *et al.* (2021) mapped >30 sills intruded into a thick succession of evaporites of Aptian age. Unfortunately, the lack of borehole calibration prevented Magee *et al.* (2021) from exploring the relationships between the intrusions and the host stratigraphy in any detail.

At a smaller scale, there have been numerous studies of mafic intrusions into evaporite deposits in salt mines and at outcrop (Knipping 1989; Schofield *et al.* 2014; Davison and Barreto 2021). These studies benefit from the smaller scale observations that can be made in mine galleries or at outcrop, but are restricted by the observational scale and lack the 3D context provided by subsurface methods.

In the case of the Dogger Sill Complex, the almost exclusive intrusion into potash-rich layers allied to the strictly concordant geometry over many tens of square kilometres is a challenge to explain without the benefit of any core data with which to examine the contact relations in more detail. Even with the limited constraints of the well and seismic data, any model for sill intrusion should explain: (1) the almost complete absence of any potash salts in wells with sill intrusions; and (2) the thickness variations in the Z3 and Z4 cycles for wells with and without sill intrusions (Fig. 6).

Gauer *et al.* (2004) suggested that the stratigraphic locus of sill intrusion at the top of the Z3 cycle was due to the replacement of the Roter Salzton, consisting of interbedded claystone, halite and potash layers. However, they based this inference on a limited well calibration set and were not able to explain how this replacement mechanism might work or test this more widely in their study area with stratigraphic correlation.

In a wider context, the preferential intrusion of sills into potash-rich layers has also been recognized in a number of salt mines in Germany (Knipping 1989). In a study of dykes and sills into the Zechstein Z1 cycle evaporites in Germany, Schofield *et al.* (2014) argued that preferential intrusion into potash seams was due to dehydration reactions involving carnallite. They suggested that these reactions could lead to localized changes in the mechanical properties (from solid to liquid) of the host evaporites ahead of the advancing intrusions and hence promote a form of ‘non-brittle’ intrusion mechanism. They described peperitic textures and halite flow into fractures in support of this mechanistic model.

Potash salts do have a lower strength, viscosity and melting temperature than halite or anhydrite (Urai 1983, 1985; Jackson and Hudec 2017) and higher bound water contents (e.g. carnallite, KCaMg $6H_2O$), so could be expected to respond very differently to contact with magma at 1100°C than halite or anhydrite. Indeed, Magee *et al.* (2021) suggested that evaporite minerals with high melting temperatures and thermal conductivities (e.g. halite, sylvite and anhydrite) will tend to fracture during rapid magma emplacement, whereas those with low dehydration temperatures and thermal conductivities (e.g. carnallite and bischofite) may behave as a fluid during intrusion and thus deform in a non-brittle fashion.

It could therefore be argued that the exploitation of the potash-rich Z3K interval in our study area is analogous to that demonstrated for the Z1 potash interval in the salt mines in Germany and that it could be primarily due to the dehydration of carnallite (Schofield *et al.* 2014). However, the large contrast in scale of these two examples means that the processes inferred to be operative in the emplacement of metre-scale intrusions in mines might not be applicable at the much larger scale of intrusions described here. In particular, the much larger thickness of the sills in the Dogger Sill Complex presents specific problems for any mechanisms involving the replacement of the original evaporite volumes by sill volume, irrespective of whether that replacement mechanism is dehydration or dissolution.

Dehydration of the Z3K potash (carnallite) could potentially achieve a volume reduction of up to 37%, but only of the net volume of carnallite (Hoff *et al.* 1912; Braitsch 1971). Because the typical net potash thicknesses in this Z3K interval rarely exceed 10–20 m (e.g. Fig. 5) (Stewart 1963; Smith and Crosby 1979), even the complete replacement of potash by magma would leave the greater proportion of the typical sill thickness (mean 53 m) to be accounted for by another mechanism (Table 1).

The dissolution of the potash seams, together with interbedded halite, could potentially have generated enough space to accommodate the intrusive volumes, but would have required a volume of unsaturated pore fluid many times the equivalent rock volume to pass through the locus of intrusion and then to leave the system. Some of the necessary water flux might have been generated by the dehydration of carnallite, but any water liberated in this way would have been in contact with >1100°C magma and would almost certainly have vaporized instantaneously (Tweto 1951; Delaney 1982; Kokelaar 1982; Kent *et al.* 1992). Under the high overpressures of the supercritical steam, it seems challenging to invoke the large volumetric dissolution of the order of 10–15 km^3 of halite and potash. It is much more likely that any volatile phases generated in the contact zone would exit the system rapidly at a high velocity via fracture networks adjacent to, or at the contact with, the dykes and contribute to the fluid flux responsible for phreatomagmatic eruptions at the upper dyke tips (Pryce *et al.* 2025).

In summary, the marked lateral variability in the thickness and distribution of the potash phases within the Z3K cycle (Figs 4, 5) is hard to reconcile with any mechanism that seeks to account for the accommodation of sill thicknesses by replacement, dehydration or dissolution of the potash phases. Instead, we favour the classical model of space creation by vertical inflation (Fig. 12). The initial propagation of the lateral tips of the sills is likely to have been from numerous discrete points along the dykes, possibly where the irregularities of the dyke walls, which are typical of many dykes, intersected with the weakest units of the stratigraphic section across which the dyke swarm was propagating (Fig. 12a). Bradley (1965) and Pollard (1973) presented examples of dykes bulging sideways as they propagated across weak clastic layers of low stiffness and Schofield *et al.* (2014) showed examples of the lateral bulging of dykes at intersections with potash seams with low stiffness. It is therefore conceivable that the dyke walls bulged into the weakest evaporite layers to initiate sill propagation at whatever potash layer was most easily exploitable within the interbedded Z3K unit.

Sill propagation may have proceeded in a self-similar geometry with inflation, or propagation may have advanced the tips ahead of inflation (cf. Cartwright *et al.* 2008; Kavanagh *et al.* 2015). Localized flow conduits may well have developed during the dominantly inflationary stage and led to salients forming in the sill perimeters (Fig. 13). Inflation would have displaced the overburden by an equivalent distance to the thickness of the intrusions, but this displacement may not have been transmitted upwards through the

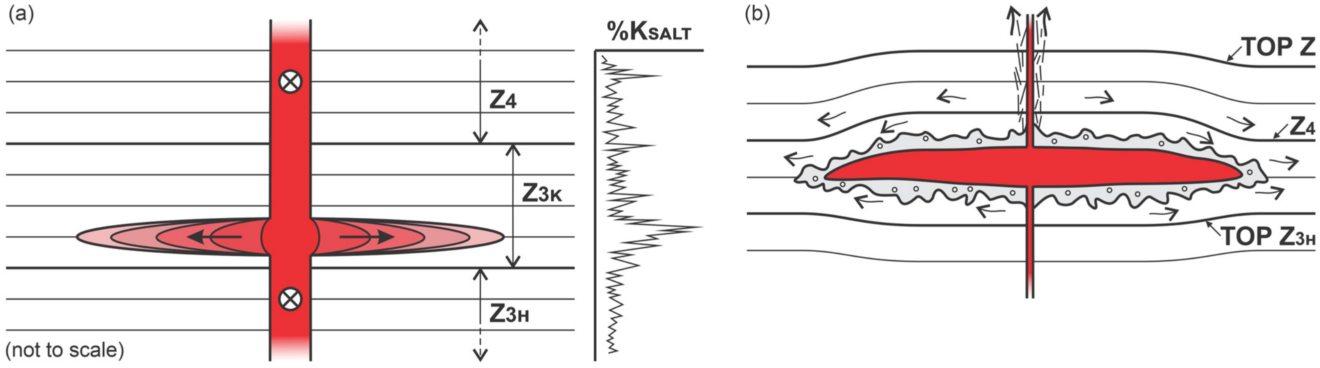

Fig. 12. Schematic diagrams showing the relationships between feeder dykes, sills and the mass balance of accommodation of sill inflationary volume. (**a**) Magma flowing via the feeder dyke as it propagates ESE (into the image) and through the Zechstein Group is intruded into the concentration of the mechanically weakest layers in Z3K, the potash-bearing interval of the uppermost Z3 cycle, indicated in a schematic plot of net potash (0–100%). The initial sill propagation may have 'budded' from the bulging lateral margins of the dyke that resulted from stiffness contrasts with the overlying and underlying purer halite units. (**b**) Propagation and inflation would elevate the overburden to some degree and possibly depress the sub-intrusion evaporites by forced folding. This active propagation/inflation phase would probably include some degree of magma–host interaction, resulting in a contact zone where dehydration, dissolution and preferential flow of the lower viscosity units would occur (grey shaded zone around the sill contacts). Steam liberated from the contact zone could exit the system via fracture networks adjacent to the dyke contacts. A recovery phase would lead to flow of mobile evaporites to eliminate any imbalances in pressure within the forcibly folded host evaporites (arrows indicate possible flow directions). Z3H, lower part of the Z3 cycle consisting dominantly of halite.

overburden because the halite and potash salts would be driven to flow to lower pressure regions on the flanks of the intrusions (Fig. 12b). The equivalent intrusive volumes of salt could therefore have flowed out of the immediately overlying and underlying contact regions of the intrusions and have been dispersed by thickening of the Zechstein in the neighbouring areas.

There would most likely have been a time lag between inflation and flow because the inflation would have to occur very rapidly on the timescale of cooling of the feeder dykes (likely weeks to months; Macdonald *et al.* 1988; Rubin 1995; Fialko and Rubin 1999), whereas salt flow of the mixed evaporite units would respond as a relaxation process to the stress induced by the sill inflation at a maximum rate of tens of centimetres per year provided the yield stress was not exceeded (Senseny *et al.* 1992; Weijermars *et al.* 1993; Jackson and Hudec 2017). It seems likely that the lateral propagation of the initial sills would also have been on a timescale of weeks to months because the dyke conduits have to remain open to feed the sills. This suggests that strain rates at the tips would be prohibitively high for any mechanism requiring viscoplastic behaviour (Köpping *et al.* 2024). If a vapour jacket developed around the sill contacts due to dehydration reactions, then it may even have acted to lubricate the contacts and speed up lateral propagation (Kent *et al.* 1992).

Given the Arrhenius dependency of many creep mechanisms with temperature within rock salt, heating of the highly conductive evaporite units surrounding the intrusions would most likely have reduced the viscosity of all the evaporite minerals and shortened this flow recovery period (Spiers *et al.* 1990; Van Keken *et al.* 1993; Urai *et al.* 2008). However, this effect is hard to quantify because there is no geothermometric data on the heat transfer surrounding sills emplaced into evaporites comparable with those available, for example, for sills intruding coal-bearing formations (Jaeger 1964; Barker *et al.* 1998; Cooper *et al.* 2007).

The thickness reduction required by the magmatic inflationary model described here is evident in all the well correlations across the Dogger Sill Complex (e.g. Fig. 4). Wherever a well intersects a sill, the Z4 cycle thickness is reduced by a measurable amount (Fig. 6). The removal by flow of the highly mobile potash-rich Z3K cycle could have completed the space accommodation requirements of the tens of metres thick sills.

Implications for the development of the MDS

The three main dyke groups of the MDS propagated for hundreds of kilometres across mainland UK and into the Southern North Sea, most likely in three separate intrusive events (Carver *et al.* 2023). The Cleveland Dyke, the southernmost of the main groups, has been estimated to have propagated 430 km over a period of days to weeks at a velocity in the range 1–5 m s^{-1} (Macdonald *et al.* 1988). These velocities are comparable with those measured from the analysis of

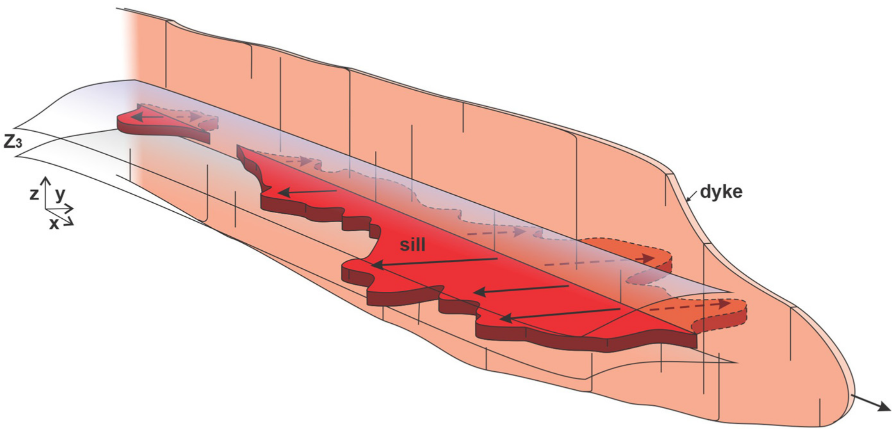

Fig. 13. Schematic illustration of dyke propagating towards its terminus and feeding a sill complex en route. Budding into various weak points at the contact between the feeder dyke and the potash-rich layer of the Z3 cycle would result in a number of discrete feeder nuclei from which the sill would propagate outwards, often asymmetrically in opposing directions, and sometimes with the development of magma flow conduits, as seen in Figure 10. This would lead to an irregular tipline geometry with numerous salients and re-entrants. Dimensions not to scale.

teleseismic data in well-instrumented modern examples of active dyke propagation (Wright *et al.* 2006; Woods *et al.* 2019). Carver *et al.* (2023) took the value of vertical height (10 km) used in the volumetric calculations of Macdonald *et al.* (1988) and extended these to the Cleveland, Blyth and Acklington dyke groups and found that cumulative dyke volumes for each of the three main groups ranged from *c.* 100 to *c.* 200 km^3.

These volumetric estimates were approximate due to the lack of constraint in the dyke widths with depth. Published dyke widths for the distal regions of the MDS are surprisingly limited, but individual dykes exposed at the surface in NE England range from 1 to 27 m thick and it is common to see a two-fold variation along the strike of any given dyke (Land 1974). To compare the relative volumes of the contributions of dykes v. sills to the total magma flux in the Blyth Dyke Group (the central group, Fig. 1b), we took the values for the aggregated dyke width of all the constituent dykes in the group assumed by Carver *et al.* (2023) and calculated the along-strike volume for a dyke height of 10 km. We co-plotted these values in bins of 17 m strike length with the across-strike sill volume (Fig. 14). The resulting plot of relative and normalized contributions shows that ratio of sill volume to dyke volume increases almost linearly up to 85 km along the Dogger Sill Complex, after which this ratio reduces to <0.3. Between 60 and 85 km along-strike, the sill volume is almost double the dyke volume (Fig. 14e).

Based on this large relative contribution of the sill volume to the gross volume of the intrusive complex, and accepting that the magma pressure must have been greater than the lithostatic pressure to lift the overburden, we suggest that the energy expenditure required to intrude and inflate the Dogger Sill Complex would have led to the loss of pressure drive within the dykes and therefore significantly reduced the flux towards the lateral tips of the central dyke group. These lateral tips extend *c.* 50 km beyond the distal limit of any mapped sills, but it might only have taken a few days at most for this ‘last gasp’ of lateral propagation before the magma ran out. The sills would have been inflating during this final stage, sequestering a large fraction of the available magma, leading to the ultimate arrest of the dykes. This loss of pressure as dykes feed sills has been observed in some analogue models and has been suggested

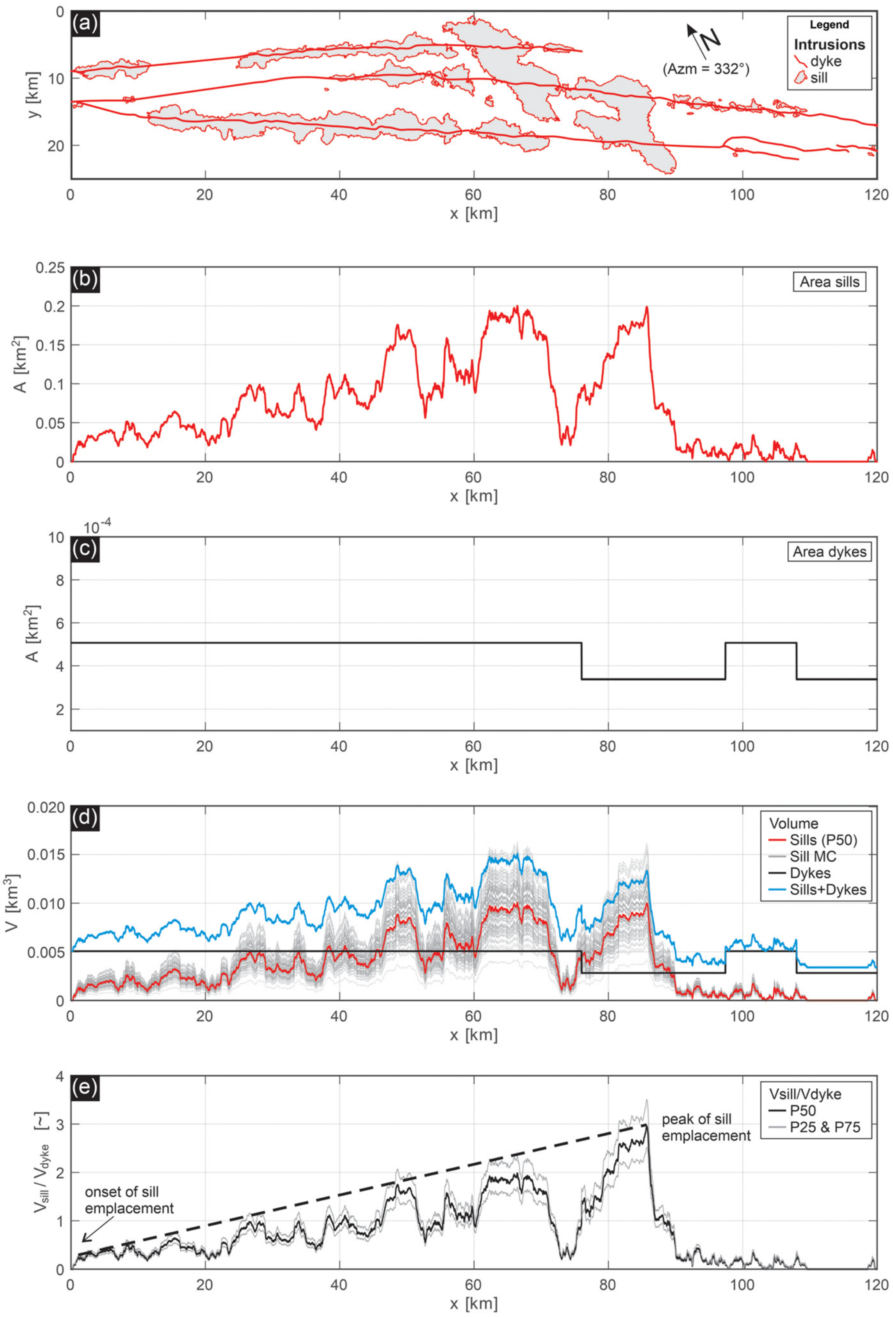

Fig. 14. Distribution, area and volumetric balance of the Dogger Sill Complex compared with the probable dyke volumes over the corresponding distance along-strike. (**a**) Location map with the central group of the Mull Dyke Swarm and the Dogger Sill Complex (relative distance in metres, bin *c.* ∼17 m, azimuth 332° N). (**b**) Plot of area shown in part (a) of the Dogger Sill Complex measured in bins of 17 m width oriented orthogonally to 332° N against distance along-strike (x). (**c**) Plot of area of the dykes shown in Figure 14a along-strike (x). (**d**) Plot of dyke volume and sill volume along-strike. The sill volume was calculated using the area of the sills and a probability distribution function based on the median and standard deviation of the calibrated sill thickness reported in Table 1. The volume values were computed in a Monte Carlo framework with a sample size N = 1E4 (only 1E3 curves are displayed) (see legend). (**e**) Volumetric ratio dykes/sills v. distance using the P25, P50 and the P75 of the sill volume previously calculated (see legend). The Dogger Sill Complex area and volume increase systematically towards the SE, with a peak in the areal extent of almost 2 km^2 and a volume of 0.01 km^3. The volumetric ratio between the dyke and sills shows a linear increase to the SE with a peak at *c.* 85 km from the onset of sill emplacement. This trend indicates a dominant supply of magma to sills over dykes. After the peak, the volumetric ratio changes rapidly, indicating a dramatic reduction in sill volume towards the SE. Dykes terminate *c.* 30 km to the SE of the box shown in part (a).

to be a probable consequence of dyke–sill interactions in magmatic systems (Kavanagh *et al.* 2015).

If correct, the Dogger Sill Complex could be viewed as a terminal sill complex, in that its emplacement effectively drained the system of the necessary energy and magma flux to continue its path any substantial distance eastwards. We cannot exclude the possibility that the termination of lateral propagation was due to the dykes encountering a mechanical barrier, but mapping by Carver *et al.* (2023) led them to suggest that no such barrier was present at or close to the lateral tips of the major dykes.

Giant dyke swarms have previously been linked to the development of sill complexes (e.g. Ernst *et al.* 1995; Palmer *et al.* 2007), but relative dyke v. sill volumetrics have not been estimated in any previous study. Magee *et al.* (2019) emphasized that the mechanics and implications of the transition from dyke swarm to sill complex have not been assessed, so it is possible that more examples of dyke-fed sill complexes will be identified as data availability allows. For example, widespread sill intrusion in the Midland Valley of Scotland and in northern England in the Late Carboniferous to Early Permian is well documented from outcrop and subsurface data. One such intrusion, the Whin Sill, has been argued to have been fed by a WNW–ESE-trending dyke swarm with an eastward extent in a dyke swarm across the North Sea (Francis 1982). Phillips *et al.* (2018) correlated this dyke swarm for *c.* 1000 km to the Farsund dyke swarm and thence to the Skaggerak large igneous province. It is therefore tempting to draw an analogy between the distally fed sills of the Midland Valley and those of the Dogger Sill Complex. Further examples of the occurrence of sills close to the terminus of giant dyke swarms may exist on Earth, and conceivably also on the other terrestrial planets, wherever giant dyke swarms form an integral part of magmatic plumbing.

Conclusions

1. The 3D seismic interpretation of high-amplitude reflections within the Zechstein Group of the South Permian Basin was calibrated with 15 wells to show that these reflections coincide with dolerite sills.
2. Six major sills were mapped in a region within 5 km of major dykes belonging to the central sub-swarm of the MDS in the UK Sector of the Southern North Sea, implying that the sills were fed by the dykes and intruded in the Late Paleocene. This newly mapped suite of sills is named the Dogger Sill Complex.
3. The sills cover a combined area of 429 km^2 and are strictly concordant and intrude within a potash-rich interval of the Z3 cycle of the Zechstein Group, suggesting a control on sill emplacement related to the physical properties of the potash units.
4. The sill thicknesses average *c.* 50 m, which rules out a dominance of space-creating mechanisms for intrusion that involve the dehydration or dissolution of potash units. Instead, sill inflation under magma pressures exceeding the lithostatic pressure best accounts for the bulk of the observed thicknesses and is consistent with changes in thickness in the host evaporites.
5. The intrusion of *c.* 22 km^3 of magma diverted from the feeding dykes to form the sills is suggested to have resulted in a substantial loss of the driving pressure in the dykes and therefore acted as a controlling factor leading to their premature arrest.

Scientific editing by Giovanni Camanni

Acknowledgements We are grateful to Schlumberger for the provision of an academic licence of Petrel. The paper contains information provided by the North Sea Transition Authority and/or other third parties. We thank David James for commenting on an earlier version of the paper and Richard Ernst for valuable discussion. We thank the reviewers Craig Magee and Jacopo Natale for their constructive comments that led to considerable improvements in the manuscript.

Author contributions **JC**: conceptualization (lead), writing – original draft (lead); **MF**: conceptualization (equal), visualization (lead), writing – original draft (equal); **DP**: data curation (lead), validation (equal), visualization (supporting), writing – review and editing (supporting).

Funding This research received no specific grant from any funding agency in the public, commercial, or not-for-profit sectors.

Competing interests The authors declare that they have no known competing financial interests or personal relationships that could have appeared to influence the work reported in this paper.

Data availability The data that support the findings of this study are available from the North Sea Transition Authority, but restrictions apply to the availability of these data, which were used under licence for the current study and so are not publicly available. Data are, however, available from the authors upon reasonable request and with permission of North Sea Transition Authority.

References

Barker, C.E., Bone, Y. and Lewan, M.D. 1998. Fluid inclusion and vitrinite-reflectance geothermometry compared to heat-flow models of maximum paleotemperature next to dikes, western onshore Gippsland Basin, Australia. *International Journal of Coal Geology*, **37**, 73–111, https://doi.org/10.1016/S0166-5162(98)00018-4

Berndt, C., Skogly, O.P., Planke, S., Eldholm, O. and Mjelde, R. 2000. High-velocity breakup-related sills in the Vøring Basin, off Norway. *Journal of Geophysical Research: Solid Earth*, **105**, 28443–28454, https://doi.org/10.1029/2000JB900217

Besly, B. 2019. Exploration and development in the Carboniferous of the Southern North Sea: a 30-year retrospective. *Geological Society, London, Special Publications*, **471**, 17–64, https://doi.org/10.1144/SP471.10

Bradley, J. 1965. Intrusion of major dolerite sills. *Transtactions of the Royal Society of New Zealand-Geology*, **3**, 27.

Braitsch, O. 1971. *Salt Deposits: Their Origin and Compositions*. Springer, New York.

Brown, A.R. 2011. *Interpretation of Three-Dimensional Seismic Data*. 7th edn. AAPG, Memoirs, **42**.

Brown, G., Platt, N.H. and McGrandle, A. 1994. The geophysical expression of Tertiary dykes in the southern North Sea. *First Break*, **12**, 137–146, https://doi.org/10.3997/1365-2397.1994011

Cameron, T.D.J., Crosby, A., Balson, P.S., Jeffrey, D.H., Lott, G.K., Bulat, J. and Harrison, D.J. 1992. *The Geology of the Southern North Sea*. United Kingdom Offshore Regional Report. British Geological Survey/HMSO, London.

Cartwright, J., James, D., Huuse, M., Vetel, W. and Hurst, A. 2008. The geometry and emplacement of conical sandstone intrusions. *Journal of Structural Geology*, **30**, 854–867, https://doi.org/10.1016/j.jsg.2008.03.012

Carver, F., Cartwright, J., McGrandle, A., Kirkham, C. and Pryce, E. 2023. The continuation of the Mull Dyke Swarm into the Southern North Sea. *Journal of the Geological Society, London*, **180**, https://doi.org/10.1144/jgs2023-039

Chambers, L.M. and Pringle, M.S. 2001. Age and duration of activity at the Isle of Mull Tertiary igneous centre, Scotland, and confirmation of the existence of subchrons during Anomaly 26r. *Earth and Planetary Science Letters*, **193**, 333–345, https://doi.org/10.1016/S0012-821X(01)00499-X

Cooper, J.R., Crelling, J.C., Rimmer, S.M. and Whittington, A.G. 2007. Coal metamorphism by igneous intrusion in the Raton Basin, CO and NM: implications for generation of volatiles. *International Journal of Coal Geology*, **71**, 15–27, https://doi.org/10.1016/j.coal.2006.05.007

Corfield, S.M., Gawthorpe, R.L., Gage, M., Fraser, A.J. and Besly, B.M. 1996. Inversion tectonics of the Variscan foreland of the British Isles. *Journal of the Geological Society, London*, **153**, 17–32, https://doi.org/10.1144/gsjgs.153.1.0017

Davison, I. and Barreto, P. 2021. Deformation and sedimentation processes, and hydrocarbon accumulations on upturned salt diapir flanks in the Lusitanian Basin, Portugal. *Petroleum Geoscience*, **27**, https://doi.org/10.1144/petgeo2019-138

Delaney, P.T. 1982. Rapid intrusion of magma into wet rock: groundwater flow due to pore pressure increases. *Journal of Geophysical Research*, **87**, 7739–7756, https://doi.org/10.1029/JB087iB09p07739

Delaney, P.T. and Pollard, D.D. 1982. Solidification of basaltic magma during flow in a dike. *American Journal of Science*, **282**, 856–885, https://doi.org/10.2475/ajs.282.6.856

El Bilali, H. and Ernst, R.E. 2024. Far-travelled 3700 km lateral magma propagation just below the surface of Venus. *Nature Communications*, **15**, 1759, https://doi.org/10.1038/s41467-024-45603-6

Ernst, R.E. and Buchan, K.L. 1997. Layered mafic intrusions: a model for their feeder systems and relationship with giant dyke swarms and mantle plume centres. *South African Journal of Geology*, **100**, 319–334, https://hdl.handle.net/10520/EJC-929df3286

Ernst, R.E., Head, J.W., Parfitt, E., Grosfils, E. and Wilson, L. 1995. Giant radiating dyke swarms on Earth and Venus. *Earth-Science Reviews*, **39**, 1–58, https://doi.org/10.1016/0012-8252(95)00017-5

Evans, A.L., Fitch, F.J. and Miller, J.A. 1973. Potassium–argon age determinations on some British Tertiary igneous rocks. *Journal of the Geological Society, London*, **129**, 419–438, https://doi.org/10.1144/gsjgs.129.4.0419

Fialko, Y.A. and Rubin, A.M. 1999. Thermal and mechanical aspects of magma emplacement in giant dyke swarms. *Journal of Geophysical Research*, **104**, 23033–23049, https://doi.org/10.1029/1999JB900213

Francis, E.H. 1982. Magma and sediment–I Emplacement mechanism of late Carboniferous tholeiite sills in northern Britain: President's anniversary address 1981. *Journal of the Geological Society, London*, **139**, 1–20, https://doi.org/10.1144/gsjgs.139.1.0001

Gauer, M.B., Upton, A.J. and McGrandle, A. 2004. Identification and interpretation of igneous sills in the Zechstein of the Southern North Sea Basin. Extended Abstract presented at PETEX, 23–25 November 2004, London.

Geikie, A. 1897. *The Ancient Volcanoes of Great Britain, Vol. 11*. Macmillan, London.

Glennie, K.W. 1986. Development of NW Europe's southern Permian gas basin. *Geological Society, London, Special Publications*, **23**, 3–22, https://doi.org/10.1144/GSL.SP.1986.023.01.01

Grant, R.J., Underhill, J.R., Hernández-Casado, J., Barker, S.M. and Jamieson, R.J. 2019. Upper Permian Zechstein Supergroup carbonate–evaporite platform palaeomorphology in the UK southern North Sea. *Marine and Petroleum Geology*, **100**, 484–518, https://doi.org/10.1016/j.marpetgeo.2017.11.029

Gudmundsson, A., Lecoeur, N., Mohajeri, N. and Thordarson, T. 2014. Dike emplacement at Bardarbunga, Iceland, induces unusual stress changes, caldera deformation, and earthquakes. *Bulletin of Volcanology*, **76**, 1–7, https://doi.org/10.1007/s00445-014-0869-8

Hansen, D.M. and Cartwright, J. 2006. Saucer-shaped sill with lobate morphology revealed by 3D seismic data: implications for resolving a shallow-level sill emplacement mechanism. *Journal of the Geological Society, London*, **163**, 509–523, https://doi.org/10.1144/0016-764905-073

Head, J.W., Crumpler, L.S., Aubele, J.C., Guest, J.E. and Saunders, R.S. 1992. Venus volcanism: classification of volcanic features and structures, associations, and global distribution from Magellan data. *Journal of Geophysical Research: Planets*, **97**, 13153–13197, https://doi.org/10.1029/92JE01273

Hoff, J.H., Precht, H., Cohen, E. and Fischer, E. 1912. *Untersuchungen über die Bildungsverhaeltnisse der ozeanischen Salzablagerungen: insbesondere des Stassfurter Salzlagers*. Akademische Verlagsgesellschaft.

Holmes, A. and Harwood, H.F. 1929. The tholeiites of the north of England. *Mineralogical Magazine and Journal of the Mineralogical Society*, **22**, 1–52, https://doi.org/10.1180/minmag.1929.022.124.03

Holness, M.B. and Humphreys, M.C.S. 2003. The Traigh Bhàn na Sgùrra sill, Isle of Mull: flow localization in a major magma conduit. *Journal of Petrology*, **44**, 1961–1976, https://doi.org/10.1093/petrology/egg066

Hughes, M. and Davison, I. 1993. Geometry and growth kinematics of salt pillows in the southern North Sea. *Tectonophysics*, **228**, 239–254, https://doi.org/10.1016/0040-1951(93)90343-I

Ishizuka, O., Taylor, R.N., Geshi, N. and Mochizuki, N. 2017. Large-volume lateral magma transport from the Mull volcano: an insight into magma chamber processes. *Geochemistry, Geophysics, Geosystems*, **18**, 1618–1640, https://doi.org/10.1002/2016GC006712

Jackson, M.P. and Hudec, M.R. 2017. *Salt Tectonics: Principles and Practice*. Cambridge University Press.

Jaeger, J.C. 1964. Thermal effects of intrusions. *Reviews of Geophysics*, **2**, 443–466, https://doi.org/10.1029/RG002i003p00443

Jenyon, M.K. 1988. Overburden deformation related to the pre-piercement development of salt structures in the North Sea. *Journal of the Geological Society, London*, **145**, 445–454, https://doi.org/10.1144/gsjgs.145.3.0445

Kavanagh, J.L., Boutelier, D. and Cruden, A.R. 2015. The mechanics of sill inception, propagation and growth: experimental evidence for rapid reduction in magmatic overpressure. *Earth and Planetary Science Letters*, **421**, 117–128, https://doi.org/10.1016/j.epsl.2015.03.038

Kemp, S.J., Smith, F.W. *et al.* 2016. An improved approach to characterize potash-bearing evaporite deposits, evidenced in North Yorkshire, United Kingdom. *Economic Geology*, **111**, 719–742, https://doi.org/10.2113/econgeo.111.3.719

Kent, R.W., Ghose, N.C., Paul, P.R., Hassan, M.J. and Saunders, A.D. 1992. Coal–magma interaction: an integrated model for the emplacement of cylindrical intrusions. *Geological Magazine*, **129**, 753–762, https://doi.org/10.1017/S0016756800008475

Kirton, S.R. and Donato, J.A. 1985. Some buried Tertiary dykes of Britain and surrounding waters deduced by magnetic modelling and seismic reflection methods. *Journal of the Geological Society, London*, **142**, 1047–1057, https://doi.org/10.1144/gsjgs.142.6.1047

Knipping, B.J. (ed.) 1989. *Basalt Intrusions in Evaporites*. Springer, Berlin.

Kokelaar, B.P. 1982. Fluidization of wet sediments during the emplacement and cooling of various igneous bodies. *Journal of the Geological Society, London*, **139**, 21–33, https://doi.org/10.1144/gsjgs.139.1.0021

Köpping, J., Magee, C., Cruden, A.R., Jackson, C.A.L. and Norcliffe, J.R. 2022. The building blocks of igneous sheet intrusions: insights from 3-D seismic reflection data. *Geosphere*, **18**, 156–182, https://doi.org/10.1130/GES02390.1

Köpping, J., Cruden, A.R., Thiele, S.T., Magee, C. and Bunger, A. 2024. Intrusion tip velocity controls the emplacement mechanism of sheet intrusions. *Geology*, **52**, 110–114, https://doi.org/10.1130/G51509.1

Land, D. 1974. *Geology of the Tynemouth District*. Memoirs of the Geological Survey of Great Britain, England and Wales (Sheet – New Series). HMSO, London.

Lister, J.R. and Kerr, R.C. 1991. Fluid-mechanical models of crack propagation and their application to magma transport in dykes. *Journal of Geophysical Research: Solid Earth*, **96**, 10049–10077, https://doi.org/10.1029/91JB00600

Macdonald, R., Wilson, L., Thorpe, R.S. and Martin, A. 1988. Emplacement of the Cleveland dyke: evidence from geochemistry, mineralogy, and physical modelling. *Journal of Petrology*, **29**, 559–583, https://doi.org/10.1093/petrology/29.3.559

Magee, C. and Jackson, C.A.L. 2020. Seismic reflection data reveal the 3D structure of the newly discovered Exmouth dyke swarm, offshore NW Australia. *Solid Earth*, **11**, 579–606, https://doi.org/10.5194/se-11-579-2020

Magee, C., Muirhead, J.D. *et al.* 2016. Lateral magma flow in mafic sill complexes. *Geosphere*, **12**, 809–841, https://doi.org/10.1130/GES01256.1

Magee, C., Ernst, R.E., Muirhead, J., Phillips, T. and Jackson, C.A.L. 2019. Magma transport pathways in large igneous provinces: lessons from combining field observations and seismic reflection data. *In:* Srivastava, R., Ernst, R. and Peng, P. (eds) *Dyke Swarms of the World: A Modern Perspective*. Springer, Singapore, 45–85, https://doi.org/10.1007/978-981-13-1666-1_2

Magee, C., Pichel, L.M., Madden-Nadeau, A.L., Jackson, C.A.L. and Mohriak, W. 2021. Salt–magma interactions influence intrusion distribution and salt tectonics in the Santos Basin, offshore Brazil. *Basin Research*, **33**, 1820–1843, https://doi.org/10.1111/bre.12537

Mège, D. and Masson, P. 1996. Amounts of crustal stretching in Valles Marineris, Mars. *Planetary and Space Science*, **44**, 749–781, https://doi.org/10.1016/0032-0633(96)00013-X

Miles, A. and Cartwright, J. 2010. Hybrid flow sills: a new mode of igneous sheet intrusion. *Geology*, **38**, 343–346, https://doi.org/10.1130/G30414.1

Mitchell, J.G., Rands, P.N. and Ineson, P.R. 1989. Perturbation of the K–Ar age system in the Cleveland dyke, U.K.: evidence of an Early Eocene age for barite mineralisation in the Magnesian Limestone of County Durham. *Chemical Geology*, **79**, 49–64, https://doi.org/10.1016/0168-9622(89)90006-7

Palmer, H.C., Ernst, R.E. and Buchan, K.L. 2007. Magnetic fabric studies of the Nippissing sill province and Senneterre dykes, Canadian Shield, and implications for emplacement. *Canadian Journal of Earth Sciences*, **44**, 507–528, https://doi.org/10.1139/E06-096

Parfitt, E.A. and Head, J.W., III 1993. Buffered and unbuffered dike emplacement on Earth and Venus: implications for magma reservoir size, depth, and rate of magma replenishment. *Earth, Moon, and Planets*, **61**, 249–281, https://doi.org/10.1007/BF00572247

Parfitt, L. and Wilson, L. 2009. *Fundamentals of Physical Volcanology*. Wiley, 33–39.

PGS Reservoir 2016. *Southern North Sea MegaSurvey*. Report **01.1343 & 04.1600/r2**, July 2016.

Phillips, T.B., Magee, C., Jackson, C.A.L. and Bell, R.E. 2018. Determining the three-dimensional geometry of a dike swarm and its impact on later rift geometry using seismic reflection data. *Geology*, **46**, 119–122, https://doi.org/10.1130/G39672.1

Pollard, D.D. 1973. Derivation and evaluation of a mechanical model for sheet intrusions. *Tectonophysics*, **19**, 233–269, https://doi.org/10.1016/0040-1951(73)90021-8

Pryce, E., Cartwright, J.A., Kirkham, C. and Phillips, D. 2025. Sequential phreatomagmatic eruptions during the lateral propagation of giant dyke swarms. *Geology*, **53**, 274–278, https://doi.org/10.1130/G52490.1

Richter-Bernburg, G. 1986. Zechstein salt correlation: England–Denmark–Germany. *Geological Society, London, Special Publications*, **22**, 165–168, https://doi.org/10.1144/GSL.SP.1986.022.01.15

Richey, J.E. 1939. The dykes of Scotland. *Transactions of the Geological Society of Edinburgh*, **13**, 393–434, https://doi.org/10.1144/transed.13.4.393

Rivalta, E., Taisne, B., Bunger, A.P. and Katz, R.F. 2015. A review of mechanical models of dike propagation: schools of thought, results and future directions. *Tectonophysics*, **638**, 1–42, https://doi.org/10.1016/j.tecto.2014.10.003

Rubin, A.M. 1995. Propagation of magma-filled cracks. *Annual Review of Earth and Planetary Sciences*, **23**, 287–336, https://doi.org/10.1146/annurev.ea.23.050195.001443

Schofield, N., Alsop, I., Warren, J., Underhill, J.R., Lehné, R., Beer, W. and Lukas, V. 2014. Mobilizing salt: magma–salt interactions. *Geology*, **42**, 599–602, https://doi.org/10.1130/G35406.1

Scott, E.D., Wilson, L. and Head, J.W., III 2002. Emplacement of giant radial dikes in the northern Tharsis region of Mars. *Journal of Geophysical Research: Planets*, **107**, 3-1–3-10, https://doi.org/10.1029/2000JE001431

Senseny, P.E., Hansen, F.D., Russell, J.E., Carter, N.L. and Handin, J.W. 1992. Mechanical behaviour of rock salt: phenomenology and micromechanisms. *International Journal of Rock Mechanics and Mining Sciences &*

Geomechanics Abstracts, **29**, 363–378, https://doi.org/10.1016/0148-9062(92)90513-Y

Smallwood, J.R. and Maresh, J. 2002. The properties, morphology and distribution of igneous sills: modelling, borehole data and 3D seismic from the Faroe–Shetland area. *Geological Society, London, Special Publications*, **197**, 271–306, https://doi.org/10.1144/GSL.SP.2002.197.01.11

Smith, D.B. 1979. Rapid marine transgressions and regressions of the upper Permian Zechstein Sea. *Journal of the Geological Society, London*, **136**, 155–156, https://doi.org/10.1144/gsjgs.136.2.0155

Smith, D.B. and Crosby, A. 1979. The regional and stratigraphical context of Zechstein 3 and 4 potash deposits in the British sector of the southern North Sea and adjoining land areas. *Economic Geology*, **74**, 397–408, https://doi.org/10.2113/gsecongeo.74.2.397

Smith, F.W., Dearlove, J.P.L., Kemp, S.J., Bell, C.P., Milne, C.J. and Pottas, T.L. 2014. Potash – recent exploration developments in North Yorkshire. *In:* Hunger, E., Brown, T. J. and Lucas, G. (eds) *Proceedings of the 17th Extractive Industry Geology Conference*, September 2012 EIG Conferences, 45–50.

Spiers, C.J., Schutjens, P.M.T.M., Brzesowsky, R.H., Peach, C.J., Liezenberg, J.L. and Zwart, H.J. 1990. Experimental determination of constitutive parameters governing creep of rocksalt by pressure solution. *Geological Society, London, Special Publications*, **54**, 215–227, https://doi.org/10.1144/GSL.SP.1990.054.01.21

Stewart, F.H. 1963. The Permian lower evaporites of Fordon in Yorkshire. *Proceedings of the Yorkshire Geological Society*, **34**, 1–44, https://doi.org/10.1144/pygs.34.1.1

Stewart, S.A. and Coward, M.P. 1995. Synthesis of salt tectonics in the southern North Sea, UK. *Marine and Petroleum Geology*, **12**, 457–475, https://doi.org/10.1016/0264-8172(95)91502-G

Strozyk, F., Van Gent, H., Urai, J.L. and Kukla, P.A. 2012. 3D seismic study of complex intra-salt deformation: an example from the Upper Permian Zechstein 3 stringer, western Dutch offshore. *Geological Society, London, Special Publications*, **363**, 489–501, https://doi.org/10.1144/SP363.23

Taylor, J.C.M. 1998. Upper Permian – Zechstein. *In:*Glennie, K.W. (ed.) *Petroleum Geology of the North Sea: Basic Concepts and Recent Advances*. Blackwell Science, 174–211.

Thomson, K. 2007. Determining magma flow in sills, dykes and laccoliths and their implications for sill emplacement mechanisms. *Bulletin of Volcanology*, **70**, 183–201, https://doi.org/10.1007/s00445-007-0131-8

Thomson, K. and Hutton, D. 2004. Geometry and growth of sill complexes: insights using 3D seismic from the North Rockall Trough. *Bulletin of Volcanology*, **66**, 364–375, https://doi.org/10.1007/s00445-003-0320-z

Trude, K.J. 2004. Kinematic indicators for shallow level igneous intrusions from 3D seismic data: evidence of flow direction and feeder location. *Geological Society, London, Memoirs*, **29**, 209–218, https://doi.org/10.1144/GSL.MEM.2004.029.01.20

Tweto, O. 1951. Form and structure of sills near Pando, Colorado. *GSA Bulletin*, **62**, 507–532, https://doi.org/10.1130/0016-7606(1951)62[507:FASOSN]2.0.CO;2

Tyrrell, G.W. 1917. Some Tertiary dykes of the Clyde area. *Geological Magazine*, **4**, 305–315, https://doi.org/10.1017/S001675680019870X

Underhill, J.R. 2009. Role of intrusion-induced salt mobility in controlling the formation of the enigmatic 'Silverpit Crater', UK Southern North Sea. *Petroleum Geoscience*, **15**, 197–216, https://doi.org/10.1144/1354-079309-843

Urai, J.L. 1983. Water assisted dynamic recrystallization and weakening in polycrystalline bischofite. *Tectonophysics*, **96**, 125–157, https://doi.org/10.1016/0040-1951(83)90247-0

Urai, J.L. 1985. Water-enhanced dynamic recrystallization and solution transfer in experimentally deformed carnallite. *Tectonophysics*, **120**, 285–317, https://doi.org/10.1016/0040-1951(85)90055-1

Urai, J.L., Schléder, Z., Spiers, C.J. and Kukla, P.A. 2008. Flow and transport properties of salt rocks. *In:* Littke, R., Bayer, U., Gajewski, D. and Nelskamp, S. (eds) *Dynamics of Complex Intracontinental Basins: the Central European Basin System*. Springer, Berlin, 277–290.

Van Keken, P.E., Spiers, C.J., Van den Berg, A.P. and Muyzert, E.J. 1993. The effective viscosity of rocksalt: implementation of steady-state creep laws in numerical models of salt diapirism. *Tectonophysics*, **225**, 457–476, https://doi.org/10.1016/0040-1951(93)90310-G

Wall, M., Cartwright, J., Davies, R. and McGrandle, A. 2010. 3D seismic imaging of a Tertiary dyke swarm in the Southern North Sea, UK. *Basin Research*, **22**, 181–194, https://doi.org/10.1111/j.1365-2117.2009.00416.x

Weijermars, R., Jackson, M.T. and Vendeville, B. 1993. Rheological and tectonic modeling of salt provinces. *Tectonophysics*, **217**, 143–174, https://doi.org/10.1016/0040-1951(93)90208-2

White, R.S. 1992. Crustal structure and magmatism of North Atlantic continental margins. *Journal of the Geological Society, London*, **149**, 841–854, https://doi.org/10.1144/gsjgs.149.5.0841

White, R.E. and Simm, R. 2003. Tutorial: good practice in well ties. *First Break*, **21**, https://doi.org/10.3997/1365-2397.21.10.25640

Widess, M.B. 1973. How thin is a thin bed? *Geophysics*, **38**, 1176–1180, https://doi.org/10.1190/1.1440403

Woods, J., Winder, T., White, R.S. and Brandsdóttir, B. 2019. Evolution of a lateral dike intrusion revealed by relatively-relocated dike-induced earthquakes: the 2014–15 Bárðarbunga–Holuhraun rifting event, Iceland. *Earth and Planetary Science Letters*, **506**, 53–63, https://doi.org/10.1016/j.epsl.2018.10.032

Wright, T.J., Ebinger, C., Biggs, J., Ayele, A., Yirgu, G., Keir, D. and Stork, A. 2006. Magma-maintained rift segmentation at continental rupture in the 2005 Afar dyking episode. *Nature*, **442**, 291–294, https://doi.org/10.1038/nature04978

Ziegler, P.A. 1990. *Geological Atlas of Western and Central Europe*. Shell Internationale Petroleum Maatschappij, The Hague.